The Astrophysical Journal, 710:903–923, 2010 February 20 doi:10.1088/0004-637X/710/2/903

CONSTRAINTS ON THE RELATIONSHIP BETWEEN STELLAR MASS AND HALO MASS AT LOW AND HIGH REDSHIFT

Benjamin P. Moster[1], Rachel S. Somerville[1,2], Christian Maulbetsch[1], Frank C. van den Bosch[1], Andrea V. Macciò[1], Thorsten Naab[3], and Ludwig Oser[3]

[1] Max-Planck-Institut für Astronomie, Königstuhl 17, 69117 Heidelberg, Germany; moster@mpia.de, maulbets@mpia.de, vdbosch@mpia.de, maccio@mpia.de
[2] Space Telescope Science Institute, 3700 San Martin Drive, Baltimore MD 21218, USA; somerville@stsci.edu
[3] Universitäts-Sternwarte München, Scheinerstr. 1, 81679 München, Germany; naab@usm.lmu.de, oser@usm.lmu.de
Received 2009 March 12; accepted 2009 December 2; published 2010 January 25

ABSTRACT

We use a statistical approach to determine the relationship between the stellar masses of galaxies and the masses of the dark matter halos in which they reside. We obtain a parameterized stellar-to-halo mass (SHM) relation by populating halos and subhalos in an *N*-body simulation with galaxies and requiring that the observed stellar mass function be reproduced. We find good agreement with constraints from galaxy–galaxy lensing and predictions of semi-analytic models. Using this mapping, and the positions of the halos and subhalos obtained from the simulation, we find that our model predictions for the galaxy two-point correlation function (CF) as a function of stellar mass are in excellent agreement with the observed clustering properties in the Sloan Digital Sky Survey at $z = 0$. We show that the clustering data do not provide additional strong constraints on the SHM function and conclude that our model can therefore predict clustering as a function of stellar mass. We compute the conditional mass function, which yields the average number of galaxies with stellar masses in the range $m \pm dm/2$ that reside in a halo of mass M. We study the redshift dependence of the SHM relation and show that, for low-mass halos, the SHM ratio is lower at higher redshift. The derived SHM relation is used to predict the stellar mass dependent galaxy CF and bias at high redshift. Our model predicts that not only are massive galaxies more biased than low-mass galaxies at all redshifts, but also the bias increases more rapidly with increasing redshift for massive galaxies than for low-mass ones. We present convenient fitting functions for the SHM relation as a function of redshift, the conditional mass function, and the bias as a function of stellar mass and redshift.

Key words: cosmology: theory – dark matter – galaxies: clusters: general – galaxies: evolution – galaxies: halos – galaxies: high-redshift – galaxies: statistics – galaxies: stellar content – large-scale structure of universe

1. INTRODUCTION

In the standard cold dark matter (CDM) paradigm, the formation of galaxies is driven by the growth of the large-scale structure of the universe and the formation of dark matter halos. Galaxies form by the cooling and condensation of gas in the centers of the potential wells of extended virialized dark matter halos (White & Rees 1978; Fall & Efstathiou 1980; Blumenthal et al. 1984). In this picture, galaxy properties, such as luminosity or stellar mass, are expected to be tightly coupled to the depth of the halo potential and thus to the halo mass.

There are various different approaches to link the properties of galaxies to those of their halos. A first method attempts to derive the halo properties from the properties of its galaxy population using, e.g., galaxy kinematics (Erickson et al. 1987; Zaritsky et al. 1993; Carlberg et al. 1996; More et al. 2009a, 2009b), gravitational lensing (Mandelbaum et al. 2005, 2006; Cacciato et al. 2009), or X-ray studies (Lin et al. 2003; Lin & Mohr 2004).

A second approach is to attempt to model the physics that shapes galaxy formation *ab initio* using either large numerical simulations including both gas and dark matter (Katz et al. 1996; Springel & Hernquist 2003) or semi-analytic models (SAMs) of galaxy formation (e.g., Kauffmann et al. 1993; Cole et al. 1994; Somerville & Primack 1999). In "hybrid" SAMs (e.g., Croton et al. 2006; Bower et al. 2006), dark matter "merger trees" are extracted from a dark matter only *N*-body simulation, and gas processes are treated with semi-analytic recipes. An advantage of this method is that high-resolution *N*-body simulations can track the evolution of individual subhalos (Klypin et al. 1999; Springel et al. 2001) and thus provide the precise positions and velocities of galaxies within a halo. However, many of the physical processes involved in galaxy formation (such as star formation and various kinds of feedback) are still not well understood, and in many cases simulations are not able to reproduce observed quantities with high accuracy.

With the accumulation of data from large galaxy surveys over the last decade, a third method has been developed, which links galaxies to halos using a statistical approach. The Halo Occupation Distribution (HOD) formalism specifies the probability distribution for a halo of mass M to harbor N galaxies with certain intrinsic properties, such as luminosity, color, or type (e.g., Peacock & Smith 2000; Seljak 2000; White 2001; Berlind & Weinberg 2002). More complex formulations of this kind of modeling, such as the conditional luminosity function (CLF) formalism (Yang et al. 2003, 2004; van den Bosch et al. 2003) have extended the HOD approach. These methods have the advantage that they do not rely on assumptions about the (poorly understood) physical processes that drive galaxy formation. In this way, it is possible to constrain the relationship between galaxy and halo properties (and thus, indirectly, the underlying physics), and to construct mock catalogs that reproduce in detail a desired observational quantity (such as the luminosity function). One disadvantage of the classical HOD approach was that one had to make assumptions about the distribution of positions and velocities of galaxies within their host halos. In addition, the results of the HOD modeling can be difficult to interpret in terms of the underlying physics of galaxy formation.

In recent years, HOD models have been introduced that make use of information about the positions, velocities, and masses of halos and subhalos extracted from a dissipationless *N*-body simulation. The (sub)halo mass is then empirically linked to

galaxy properties by requiring that a statistical observational quantity (e.g., galaxy luminosity function and/or galaxy two-point correlation function) is reproduced. This is either done by assuming parameterized functions to relate galaxy properties (such as luminosity) to halo mass or by assuming a non-parametric monotonic relation. It has been shown that these simple models reproduce galaxy clustering as a function of luminosity over a wide range in redshift (Kravtsov et al. 2004; Tasitsiomi et al. 2004; Tinker et al. 2005; Vale & Ostriker 2006; Conroy et al. 2006; Shankar et al. 2006; Wang et al. 2006; Marín et al. 2008).

Observationally, it is well known that galaxy clustering is a function of spatial scale, galaxy properties (such as luminosity and type), and redshift. Luminous (massive) galaxies are more strongly clustered than less luminous (less massive) galaxies (Norberg et al. 2001, 2002; Zehavi et al. 2002, 2005; Li et al. 2006). One can split the galaxy two-point correlation function (2PCF) into two separate parts: the one-halo and the two-halo terms. The one-halo term, which dominates on small scales, depends strongly on the galaxy distribution within the halo as well as the details of the HOD. The two-halo term, which dominates on scales that are much larger than a typical halo, is proportional to the auto-correlation of the halo population. In general, the two terms are not expected to combine to produce a featureless power law, but generally show a break or dip at the scale where the transition from the one-halo to the two-halo term occurs (Zehavi et al. 2004).

The extensive multi-wavelength spectrophotometric information that is now available for large numbers of galaxies allows us to estimate physical parameters of galaxies, such as stellar masses, instead of relying on observational properties such as magnitudes (Bell & de Jong 2001; Kauffmann et al. 2003; Panter et al. 2004). These estimates can even be obtained—with a proper measure of caution—for high-redshift galaxies. Stellar mass estimates have been presented in the literature for galaxies up to redshifts as high as $z \sim 6$ (Yan et al. 2006; Eyles et al. 2007), and stellar mass function (SMF) estimates have been presented up to $z \sim 5$ (Drory et al. 2005; Fontana et al. 2006; Elsner et al. 2008). The goal of our paper is to develop a "Conditional Stellar Mass Function" (CMF) formalism, which is the stellar mass analog of the CLF. The CMF yields the average number of galaxies with stellar masses in the range $m \pm dm$ as a function of the host halo mass M and can be regarded as the SMF for halos of mass M. We apply this formalism at low redshift and up to the highest redshifts where reliable observational stellar mass estimates are available ($0.1 \lesssim z \lesssim 4$). In this way, we derive a parameterized relationship between dark matter halo mass and galaxy mass as a function of redshift.

Using a parameterized relationship has several advantages. First, it provides a convenient way for other researchers to make use of our results and obtain an expression for stellar mass as a function of halo mass. Second, it is straightforward to include scatter in the relation, which is physically more realistic: one just has to choose a number drawn from an assumed random distribution and add that to the average relation. Finally, it is straightforward to treat central and satellite galaxies separately and assume different relations between stellar and halo mass for those populations. However, here we make the assumption that both populations follow the same relation, which has consequences for the clustering predictions of our model.

Using the CMF derived *only* from constraints from the observed SMF, we compute the predicted (projected) galaxy CF at $z \sim 0$ as a function of stellar mass, and find good agreement with the observational results of Li et al. (2006). Furthermore, we show that assuming central and satellite galaxies follow the same relation between stellar and halo mass, adding the clustering constraints does not tighten the constraints on our model parameters; i.e., any model that satisfies the mass function constraints will produce the correct clustering. Based on this result, we use our redshift-dependent CMF results to *predict* the clustering as a function of stellar mass and redshift. To date, observational measurements of clustering as a function of stellar mass have only been published for $z \lesssim 1$ (Meneux et al. 2008, 2009). We show that our model predictions agree very well with these measurements. Very soon it will be possible to test our predictions for redshifts beyond $z = 1$ with the results from deep wide-field surveys (e.g., MUSYC, UKIDDS, etc.). We again present convenient fitting functions for the galaxy bias as a function of both stellar mass and redshift. In a forthcoming companion paper (Moster et al. 2010), we employ our estimates of galaxy bias in order to compute the "cosmic variance," the uncertainty in observational estimates of the volume density of galaxies arising from the underlying large-scale density fluctuations.

This paper is organized as follows. In Section 2, we describe the N-body simulation, the halo finding algorithm that was used to obtain a halo catalog and the treatment of "orphaned" galaxies. Section 3 specifies our model: we motivate the form of the stellar-to-halo mass (SHM) relation and constrain it by requiring that the observed SMF is reproduced. The clustering properties of galaxies are then inferred from those of the halo population. We discuss the meaning of the parameters of the SHM relation and demonstrate that clustering puts only weak constraints on them. In Section 5, we introduce the CMF, which describes how halos are occupied by galaxies, and compute the occupation numbers. Section 6 gives a comparison between our results and several other models and observations. In Section 7, we apply our method to higher redshifts and determine the redshift dependence of the SHM relation. We make predictions of the stellar mass dependent galaxy CF at higher redshift, which we use to compute the galaxy bias. Finally, we summarize our methods and conclusions in Section 8.

Throughout this paper, we assume a ΛCDM cosmology with $(\Omega_m, \Omega_\Lambda, h, \sigma_8, n) = (0.26, 0.74, 0.72, 0.77, 0.95)$. We employ a Kroupa (2001) initial mass function (IMF) and convert all stellar masses to this IMF. In order to simplify the notation, we will use the capital M to denote dark matter halo masses and the lower case m to denote galaxy stellar masses.

2. THE SIMULATION AND HALO CATALOGS

High-resolution dissipationless N-body simulations have shown that distinct halos[4] contain subhalos which orbit within the potential of their host halo. These subhalos were distinct halos in the past, and entered the larger halo via merging during the process of hierarchical assembly. We will refer to the galaxy at the center of a distinct halo as a central galaxy, and the galaxies within subhalos as "satellites;" and we will use the term "halo" to refer to the distinct halo for central galaxies and to the subhalo in which the galaxy originally formed for satellite galaxies.

*A*b initio models of galaxy formation predict that the stellar mass of a galaxy is tightly correlated with the depth of the potential well of the halo in which it formed. For distinct halos,

[4] We refer to virialized halos that are not subhalos of another halo as "distinct."

the relevant mass is the virial mass at the time of observation. Subhalos, however, lose mass while orbiting in a larger system as their outer regions are tidally stripped. Stars are centrally concentrated and more tightly bound than the dark matter, however, and so the stellar mass of a galaxy which is accreted by a larger system probably changes only slightly until most of the dark matter has been stripped off. Therefore, the subhalo mass at the time of observation is probably not a good tracer for the potential well that shaped the galaxy properties. A better tracer is the subhalo mass at the time that it was accreted by the host halo, or its maximum mass over its history.[5] This was first proposed by Conroy et al. (2006).

The population of dark matter halos used in this work is drawn from an *N*-body simulation run with the simulation code GADGET-2 (Springel 2005) on a SGI AltixII at the University Observatory Munich. The cosmological parameters of the simulation are chosen to match results from WMAP-3 (Spergel et al. 2007) for a flat ΛCDM cosmological model: $\Omega_m = 0.26$, $\Omega_\Lambda = 0.74$, $h = H_0/(100\ \mathrm{km\ s^{-1}\ Mpc^{-1}}) = 0.72$, $\sigma_8 = 0.77$, and $n = 0.95$. The initial conditions were generated using the GRAFIC software package (Bertschinger 2001). The simulation was done in a periodic box with side length 100 Mpc, and contains 512^3 particles with a particle mass of $2.8 \times 10^8\ M_\odot$ and a force softening of 3.5 kpc.

Dark matter halos are identified in the simulation using a friends-of-friends (FoF) halo finder. Substructures inside the FoF groups are then identified using the SUBFIND code described in Springel et al. (2001). For the most massive subgroup in a FoF group, the virial radius and mass are determined with a spherical overdensity criterion: the density inside a sphere centered on the most bound particle is required to be greater than or equal to the value predicted by the spherical collapse model for a tophat perturbation in a ΛCDM cosmology (Bryan & Norman 1998). As discussed above, for subhalos we use the maximum mass over its past history, which is typically the mass when the halo was last a distinct halo and did not yet overlap with its later host. Merger trees were constructed out of the halo catalogs at 94 time steps, equally spaced in expansion factor ($\Delta a = 0.01$), based on the particle overlap of halos at different time steps.

Due to the finite mass resolution of the simulation ($M_{\mathrm{min,halo}} \simeq 10^{10}\ M_\odot$), subhalos can no longer be identified when their mass has dropped below this limit due to tidal stripping. Since mass loss can be substantial (>90%) this is important even for fairly massive subhalos. A special treatment of these so-called "orphans" is necessary. We determine the orbital parameters at the last moment when a subhalo is identified in the simulation and use them in the dynamical friction recipe of Boylan-Kolchin et al. (2008), which is applicable at radii $r < r_{\mathrm{vir}}$. We also tried an alternate recipe in which we make no explicit use of the subhalo information, but apply the dynamical friction formula from the time when the satellites first enter the host halo. We obtained very similar subhalo mass functions and radial distributions with the alternate recipe, confirming the self-consistency of the approach.

For the halo positions in the determination of CFs, we use the coordinates of the most bound particle for distinct and subhalos. For orphans, by definition, the position is not known, so we follow the position of the most bound particle from the last time step when a subhalo was identified. Since the dynamical friction force vanishes in the dark matter only simulation after a subhalo is dissolved, yet not in reality when a galaxy is present at the center of the subhalo, the distance to the center of the host halo might be slightly overestimated with this prescription.

[5] In an idealized situation, halo mass should increase monotonically with time until the halo becomes a subhalo, at which point the mass begins to decrease due to tidal stripping.

3. CONNECTING GALAXIES AND HALOS

In this section, we describe how we derive the relationship connecting the stellar mass of a galaxy to the mass of its dark matter halo. In the standard picture of galaxy formation, gas can only cool and form stars if it is in a virialized gravitationally bound dark matter halo (White & Rees 1978). In this model, the gas cooling rate, the star formation rate, and thus the properties of the galaxy depend mainly on the virial mass of the host halo. Thus, we expect the stellar mass of a central galaxy to be strongly correlated with the virial mass of the halo in which the galaxy formed. As we discussed in the last section, this corresponds to the virial mass for central galaxies, and to the maximum mass over the halo's history for satellite galaxies. In the rest of this work, unless noted otherwise, the halo mass M will represent:

$$M = \begin{cases} M_{\mathrm{vir}}, & \text{for host halos} \\ M_{\mathrm{max}}, & \text{for subhalos} \end{cases} . \quad (1)$$

Note that we have also experimented with instead using the present mass for subhalos, and found that we were not able to reproduce the galaxy clustering properties (see also Conroy et al. 2006).

3.1. The Stellar-to-halo Mass Relation

In order to link the stellar mass of a galaxy m to the mass of its dark matter halo M, we need to specify the SHM ratio. A direct comparison of the halo mass function $n(M)$ and the galaxy mass function $\phi(m)$ helps to constrain the SHM function. If we assume that every host (sub) halo contains exactly one central (satellite) galaxy and that each system has exactly the same SHM ratio m/M, the galaxy SMF can be derived trivially from the halo mass function and has the same features. The galaxy mass function derived for $m/M = 0.05$ is compared to the observed Sloan Digital Sky Survey (SDSS) galaxy mass function in Figure 1. The observed galaxy mass function is steeper for high masses and shallower for low masses than the one derived from the halo mass function. Thus, for a constant SHM ratio there will inevitably be too many galaxies at the low and high mass end.

This implies that the actual SHM ratio m/M is not constant, but increases with increasing mass, reaches a maximum around m^* and then decreases again. Hence, we adopt the following parameterization, similar to the one used in Yang et al. (2003):

$$\frac{m(M)}{M} = 2\left(\frac{m}{M}\right)_0 \left[\left(\frac{M}{M_1}\right)^{-\beta} + \left(\frac{M}{M_1}\right)^{\gamma}\right]^{-1} . \quad (2)$$

It has four free parameters: the normalization of the SHM ratio $(m/M)_0$, a characteristic mass M_1, where the SHM ratio is equal to $(m/M)_0$, and two slopes β and γ which indicate the behavior of m/M at the low and high mass ends, respectively. We use the same parameters for the central and satellite populations, since—unlike luminosity—the stellar mass of satellites changes only slightly after they are accreted by the host halo.

Note that though both β and γ are expected to be positive, they are not restricted to be so. The SHM relation is therefore not necessarily monotonic.

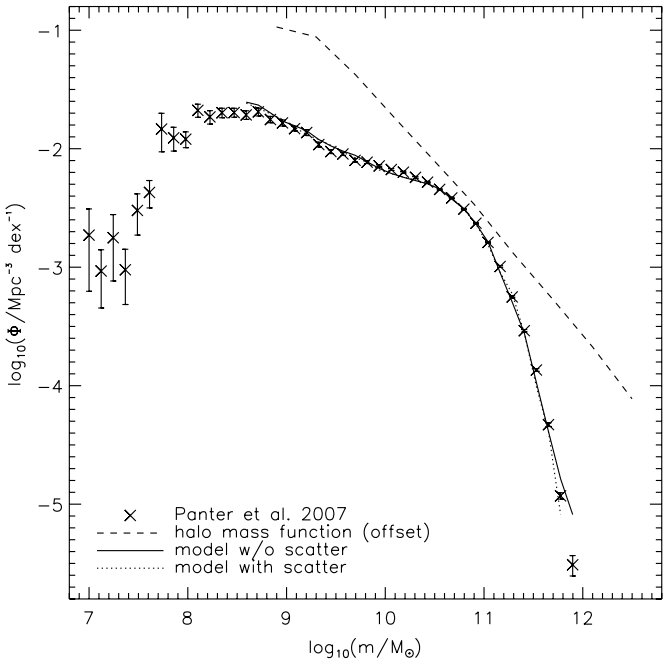

Figure 1. Comparison between the halo mass function offset by a factor of 0.05 (dashed line), the observed galaxy mass function (symbols), our model without scatter (solid line), and our model including scatter (dotted line).We see that the halo and the galaxy mass functions are different shapes, implying that the stellar-to-halo mass ratio m/M is not constant. Our four-parameter model for the halo mass dependent stellar-to-halo mass ratio is in very good agreement with the observations (both including and neglecting scatter).

3.2. Constraining the Free Parameters

Having set up the model, we now need to constrain the four free parameters M_1, $(m/M)_0$, β, and γ. To do this, we populate the halos in the simulation with galaxies. The stellar masses of the galaxies depend on the mass of the halo and are derived according to our prescription (Equation (2)). The positions of the galaxies are given by the halo positions in the N-body simulation.

Once the simulation box is filled with galaxies, it is straightforward to compute the SMF $\Phi_{\rm mod}(m)$. As we want to fit this model mass function to the observed mass function $\Phi_{\rm obs}(m)$ by Panter et al. (2007), we choose the same stellar mass range ($10^{8.5}\,M_\odot$–$10^{11.85}\,M_\odot$) and the same bin size. The observed SMF was derived using spectra from the Sloan Digital Sky Survey Data Release 3 (SDSS DR3); see Panter et al. (2004) for a description of the method.

Furthermore, it is possible to determine the stellar mass dependent clustering of galaxies. For this, we compute projected galaxy CFs $w_{p,\rm mod}(r_p, m_i)$ in several stellar mass bins which we choose to be the same as in the observed projected galaxy CFs of Li et al. (2006). These were derived using a sample of galaxies from the SDSS DR2 with stellar masses estimated from spectra by Kauffmann et al. (2003).

We first calculate the real space CF $\xi(r)$. In a simulation, this can be done by simply counting pairs in distance bins:

$$\xi(r_i) = \frac{dd(r_i)}{N_p(r_i)} - 1, \tag{3}$$

where $dd(r_i)$ is the number of pairs counted in a distance bin and $N_p(r_i) = 2\pi N^2 r_i^2 \Delta r_i / L_{\rm box}^3$, where N is the total number of galaxies in the box. The projected CF $w_p(r_p)$ can be derived by integrating the real space correlation function $\xi(r)$ along the line of sight:

$$w_p(r_p) = 2\int_0^\infty dr_{||}\,\xi\left(\sqrt{r_{||}^2 + r_p^2}\right) = 2\int_{r_p}^\infty dr\,\frac{r\xi(r)}{\sqrt{r^2 - r_p^2}}\,, \tag{4}$$

where the comoving distance (r) has been decomposed into components parallel ($r_{||}$) and perpendicular (r_p) to the line of sight. The integration is truncated at 45 Mpc. Due to the finite size of the simulation box ($L_{\rm box} = 100$ Mpc), the model correlation function is not reliable beyond scales of $r \sim 0.1 L_{\rm box} \sim 10$ Mpc.

In order to fit the model to the observations, we use Powell's directions set method in multidimensions (e.g., Press et al. 1992) to find the values of M_1, $(m/M)_0$, β, and γ that minimize either

$$\chi_r^2 = \chi_r^2(\Phi) = \frac{\chi^2(\Phi)}{N_\Phi}$$

(mass function fit) or

$$\chi_r^2 = \chi_r^2(\Phi) + \chi_r^2(w_p) = \frac{\chi^2(\Phi)}{N_\Phi} + \frac{\chi^2(w_p)}{N_r\ N_m}$$

(mass function and projected CF fit) with N_Φ and N_r the number of data points for the SMF and projected CFs, respectively, and N_m the number of mass bins for the projected CFs.

In this context, $\chi^2(\Phi)$ and $\chi^2(w_p)$ are defined as follows:

$$\chi^2(\Phi) = \sum_{i=1}^{N_\Phi}\left[\frac{\Phi_{\rm mod}(m_i) - \Phi_{\rm obs}(m_i)}{\sigma_{\Phi_{\rm obs}(m_i)}}\right]^2,$$

$$\chi^2(w_p) = \sum_{i=1}^{N_m}\sum_{j=1}^{N_r}\left[\frac{w_{p,\rm mod}(r_{p,j}, m_i) - w_{p,\rm obs}(r_{p,j}, m_i)}{\sigma_{w_{p,\rm obs}(r_{p,j}, m_i)}}\right]^2,$$

with $\sigma_{\Phi_{\rm obs}}$ and $\sigma_{w_{p,\rm obs}}$ the errors for the SMF and projected CFs, respectively. Note that for the simultaneous fit, by adding the reduced χ_r^2, we give the same weight to both data sets.

3.3. Estimation of Parameter Errors

In order to obtain estimates of the errors on the parameters, we need their probability distribution prob($A|I$), where A is the parameter under consideration and I is the given background information. The most likely value of A is then given by: $A_{\rm best} = \max(\text{prob}(A|I))$.

As we have to assume that all our parameters are coupled, we can only compute the probability for a given set of parameters. This probability is given by:

$$\text{prob}(M_1, (m/M)_0, \beta, \gamma|I) \propto \exp(-\chi^2).$$

In a system with four free parameters A, B, C, and D one can calculate the probability distribution of one parameter (e.g., A) if the probability distribution for the set of parameters is known, using marginalization:

$$\begin{aligned}\text{prob}(A|I) &= \int_{-\infty}^{\infty}\text{prob}(A, B|I)dB \\ &= \int_{-\infty}^{\infty}\text{prob}(A, B, C, D|I)dBdCdD.\end{aligned}$$

Once the probability distribution for a parameter is determined, one can assign errors based on the confidence intervals.

Table 1
Fitting Results for Stellar-to-halo Mass Relationship

	$\log M_1$	$(m/M)_0$	β	γ	$\chi_r^2(\Phi)$	$\chi_r^2(w_p)$
Best fit	11.884	0.02820	1.057	0.556	1.56	3.83
σ^+	0.030	0.00061	0.054	0.010		
σ^-	0.023	0.00053	0.046	0.004		

Notes. No scatter included. All masses are in units of $M_\odot$.

This is the shortest interval that encloses a certain percentage X of the area under the posterior probability distribution. For the 1σ error $X = 68\%$, while for the 2σ error $X = 95\%$. Assuming that the probability distribution has been normalized to have unit area we seek A_1 and A_2 such that

$$\int_0^{A_1} \mathrm{prob}(A|I)dA = \int_{A_2}^{\infty} \mathrm{prob}(A|I)dA = \frac{1-X}{2}.$$

Finally, the parameter A is given as $A = A_{\mathrm{best}}{}^{+\sigma_+}_{-\sigma_-}$ with $\sigma_+ = A_2 - A_{\mathrm{best}}$ and $\sigma_- = A_{\mathrm{best}} - A_1$. The errors derived in this way only include sources that have been considered when computing χ^2. The calculation of the errors applies for uncorrelated data points. Since in our case the data points are correlated, the values of the errors are slightly modified. Also errors caused by cosmic variance are not included.

4. FITTING RESULTS

Here we present the results we obtain by fitting to the SMF only, and for the combined fit to the SMF and the projected CF.

4.1. The Stellar Mass Function Fit

First, we fit to the SDSS SMF and use the derived best-fit parameters to calculate the model projected correlation functions. Note that for now, we do not take into account any possible scatter in the $m(M)$ relation. We will consider scatter in Section 4.5.

We see in Figure 1 that our fit produces excellent agreement with the observed SMF. Using the approach described above we also compute the errors on the parameters. The results are summarized in Table 1.

Having derived the best-fit parameters, we can predict the projected CFs. We present the results both including and not including orphan galaxies, where we have fitted to the SMF for each case.

Figure 2 shows a comparison between our model and the SDSS projected correlation functions in five stellar mass bins ranging from $\log m/M_\odot = 9.0$ to $\log m/M_\odot = 11.5$ with a bin size of 0.5 dex. The correlation function that has been derived without orphans is too low at small scales and can be regarded as a lower limit. Neglecting these galaxies results in an underprediction of satellite galaxy clustering. As on small scales, the projected CF depends mainly on the one-halo term this results in the underprediction of $w_p(r_p)$. This effect weakens for the clustering of more massive galaxies as they are more likely to be central galaxies and thus not effected by tidal stripping at all.

The agreement with the observationally derived $w_p(r_p)$ for the catalog including orphaned galaxies is very good, which is also reflected in the low value of $\chi_r^2(w_p) = 3.83$. Note that this value has been calculated with the parameters from the mass function fit given above and does not correspond to a fit to the projected CFs.

Note that we plot the projected CFs only up to 20 Mpc. Because of the finite box size, the clustering of host halos and thus central galaxies is underpredicted at large scales independent of mass. Additionally, due to the lack of long-wavelength modes, massive halos, and galaxies can be underproduced leading to an underprediction of w_p for the massive objects, independent of scale. However, the latter effect is very small, since the abundance of the massive halos in our simulation agrees very well with the predicted average (Sheth & Tormen 1999).

As a test we also used the present mass instead of the maximum mass for subhalos. We then found that the projected CF was particularly underpredicted on small scales. This effect is due to tidal stripping of subhalos and is thus strongest at small scales where the subhalo contribution dominates.

4.2. The Combined Fit

We now investigate whether we can improve the agreement between the model and the observed projected CFs by performing a combined fit as described above. We obtain the same parameters as those we derived from the fit to the SMF alone. This seems surprising, but on further inspection we find that this is due to $\chi^2(m)$ being a lot more sensitive to changes of the parameters than $\chi^2(w_p)$. This means that if one changes the parameters a little in order to improve the fit to the projected correlation functions, one can get a slightly better agreement between the model and the observed projected CFs only at the cost of a large disagreement between the model and the observed SMFs. In other words: $\chi^2(w_p)$ is much flatter around its minimum than $\chi^2(w_p)$, as shown in Figure 3.

This means that, assuming that both central and satellite galaxies follow the same SHM relation, the model that matches the SMF can reproduce the correct clustering. However, if subhalos have a different SHM ratio there is an infinite number of solutions that match the SMF but produce very different correlation functions. The only way to constrain the SHM relations then is to take the clustering data into account. By adopting different SHM relations for central and satellite populations it is even possible to produce a slightly better fit to the correlation functions (Wang et al. 2006).

On the other hand, if one wants to *predict* clustering as a function of stellar mass (e.g., at higher redshift) then one has to make an assumption about how the SHM ratios of central and satellite galaxies are related. We made the very simple assumption, that the relation between the stellar mass of central galaxies and the virial mass of their host halo and the relation between the stellar mass of satellite galaxies and the mass of the subhalo at the time of accretion is the same, and have shown that this leads to very good predictions for the mass dependent clustering. We conclude that under this simple assumption we can use our model to predict clustering as a function of stellar mass.

4.3. The Resulting Stellar-to-halo Mass Relation

The upper panel of Figure 4 shows the derived stellar mass as a function of halo mass. The light shaded area gives the 68% confidence interval, while the dark and light shaded areas together give the 95% confidence interval. These have been derived using a set of different models computed on a mesh, as described in Section 3.3.

For the SHM ratio, we apply the same procedure. The result is shown in the lower panel of Figure 4. We see that the SHM ratio has the form we expected: it increases with increasing halo

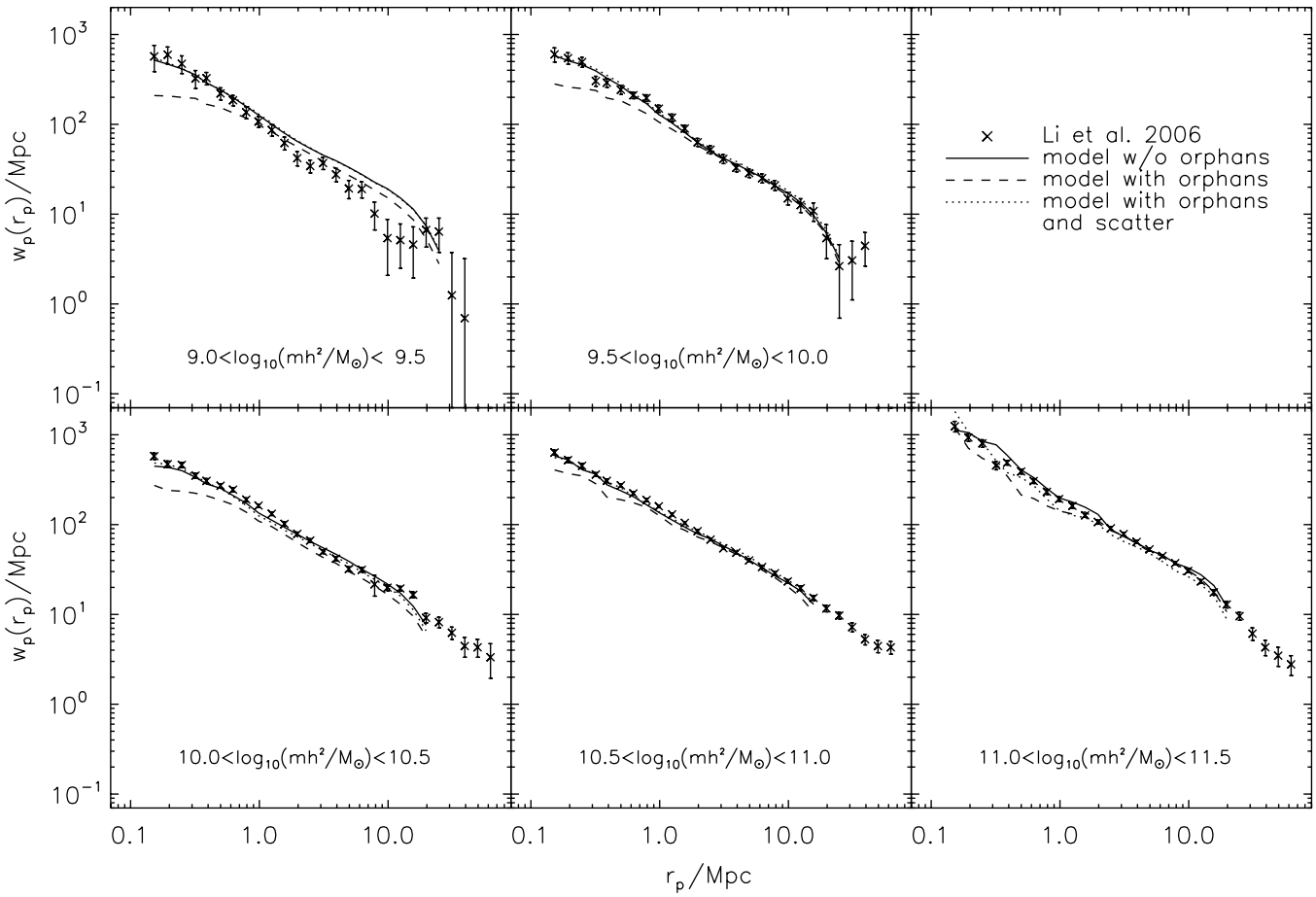

Figure 2. Comparison between the model (lines) and observed (symbols with error bars) projected correlation functions. We show the model results both including (solid) and excluding (dashed) orphan galaxies. The models have been derived by fitting to the stellar mass function only.

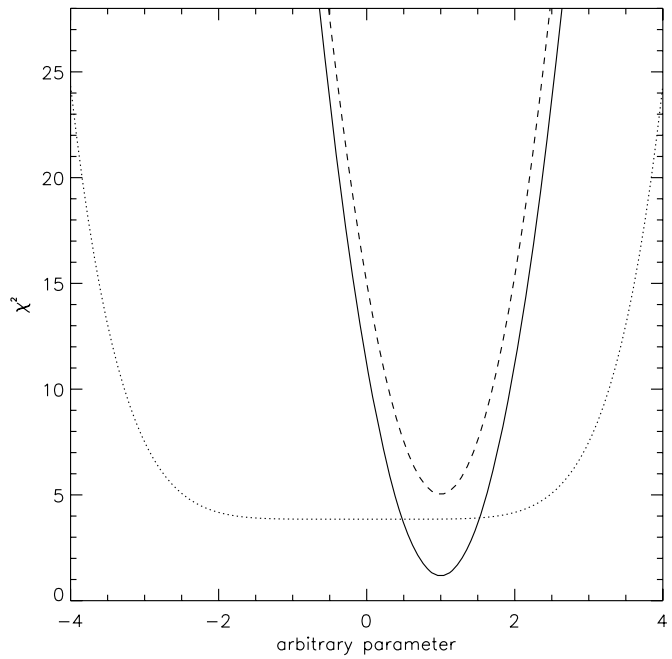

Figure 3. Sketch of the probability distributions for a simultaneous fit. The solid line corresponds to $\chi^2(m)$ and the dotted line to $\chi^2(w_p)$. The dashed line is the sum of both. Since $\chi^2(w_p)$ is flat at the minimum, $\chi^2_{\rm tot}$ follows $\chi^2(m)$ with an offset. The resulting probability distribution does not change (after normalization).

mass, reaches its maximum value around M_1 and then decreases again.

4.4. Meaning of Parameters and Correlations

We now explore the effects of changing each parameter in order to understand how they affect the SMF. If we keep M_1, β, and γ fixed and only vary $(m/M)_0$, this corresponds to changing the stellar mass of the galaxy that lives inside each halo by a constant factor. This has no impact on the form of the SMF. Its shape stays the same, while only the position on the stellar mass axis changes. Due to the monotonic form of the SMF, this directly determines the value of the normalization ϕ^*. For a larger value of $(m/M)_0$, we get a larger value of ϕ^*.

Varying only M_1, we find that the shape of the SMF changes drastically. For a higher M_1 than our best-fit value, we get too many massive galaxies and too few low mass galaxies, while for a lower value of M_1 we get too few massive galaxies and too many low mass galaxies. This is because M_1 is the characteristic mass corresponding to the highest SHM ratio. In the SMF, this corresponds to the knee and we get a SMF which has its knee at the stellar mass corresponding to M_1. For a larger M_1, the knee is shifted to a higher stellar mass. Together, M_1 and the maximum SHM ratio $(m/M)_0$ determine the normalization of the SMF ϕ and the characteristic mass m^*.

Changing β affects mainly the low-mass slope of the SMF. For larger values of β, the slope becomes shallower. As β influences

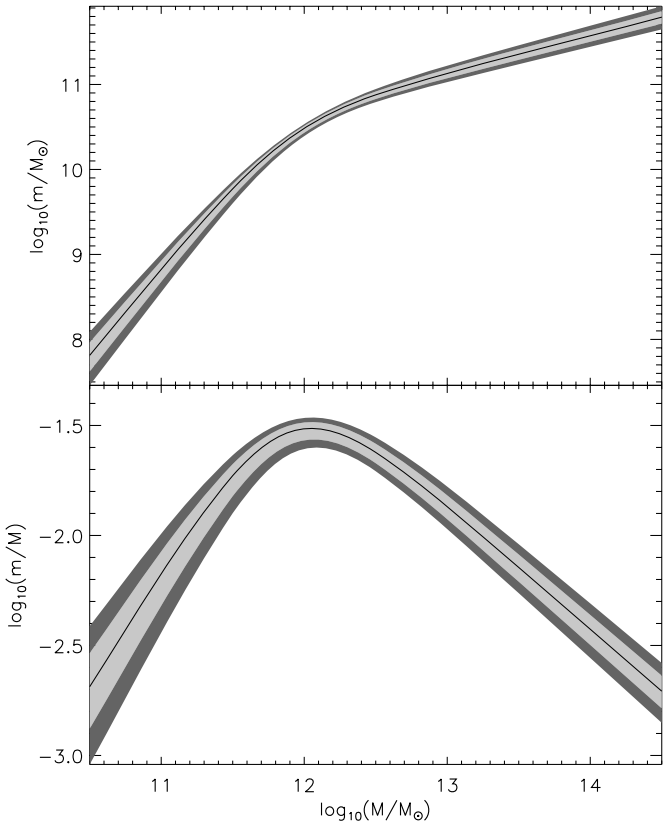

Figure 4. Derived relation between stellar mass and halo mass. The light shaded area shows the 1σ region while the dark and light shaded areas together show the 2σ region. The upper panel shows the SHM relation, while the lower panel shows the SHM ratio.

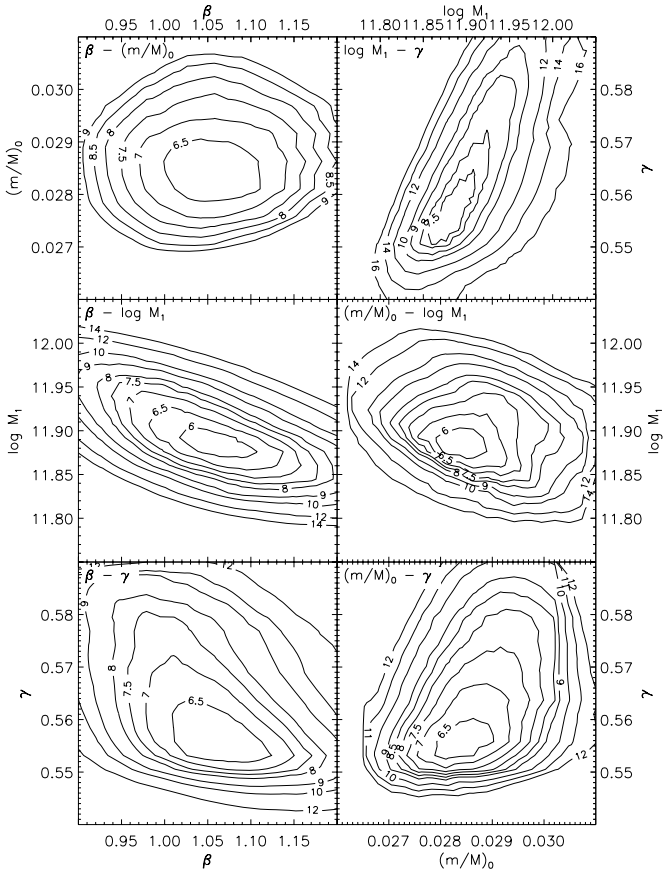

Figure 5. Correlations between the model parameters. The panels show contours of constant χ^2 (i.e., constant probability) for the fit including constraints from the SMF only. The parameter pairs are indicated in each panel.

mainly the slope of the low mass end of the SMF, it is strongly related to the parameter α of the Schechter function. A small value of β corresponds to a high value of α.

If we change γ, this mainly impacts the slope of the massive end of the SMF. For larger values of γ than for its best-fit value, the slope of the massive end becomes steeper. As γ affects mainly the slope of the massive end of the SMF, it is not coupled to a parameter of the Schechter function though it is related to the high-mass cutoff, assumed to be exponential in a Schechter function.

Figure 5 shows the contours of the two-dimensional probability distributions for the parameters pairs. We see a correlation between the parameters $[M_1, \gamma]$ and $[(m/M)_0, \gamma]$ and an anti-correlation between $[\beta, \gamma]$, $[\beta, M_1]$, and $[(m/M)_0, M_1]$. There does not seem to be a correlation between $[\beta, (m/M)_0]$.

4.5. Introducing Scatter

Up until now we have assumed that there is a one-to-one, deterministic relationship between halo mass and stellar mass. However, in nature, we expect that two halos of the same mass M may harbor galaxies with different stellar masses, since they can have different halo concentrations, spin parameters, and merger histories.

For each halo of mass M, we now assign a stellar mass m drawn from a lognormal distribution with a mean value given by our previous expression for $m(M)$ (Equation (2)), with a variance of σ_m^2. We assume that the variance is a constant for all halo masses, which means that the percent deviation from m is the same for every galaxy. This is consistent with other halo occupation models, SAMs and satellite kinematics (Cooray 2006; van den Bosch et al. 2007; More et al. 2009b).

Table 2
Fitting Results for Stellar-to-halo Mass Relationship

	log M_1	$(m/M)_0$	β	γ	$\chi_r^2(\Phi)$	$\chi_r^2(w_p)$
Best fit	11.899	0.02817	1.068	0.611	1.42	4.21
σ^+	0.026	0.00063	0.051	0.012		
σ^-	0.024	0.00057	0.044	0.010		

Notes. Including scatter $\sigma_m = 0.15$. All masses are in units of $M_\odot$.

Assuming a value of $\sigma_m = 0.15$ dex and fitting the SMF only, we find the values given in Table 2. These values lie within the (2σ) error bars of the best-fit values that we obtained with no scatter. The largest change is on the value of γ, which controls the slope of the SHM relation at large halo masses. The SMF and the projected CFs for the model including scatter are shown in Figures 1 and 2, respectively, and show very good agreement with the observed data.

In Figure 6, we compare our model without scatter with the model including scatter. We have also included the relation between halo mass and the average stellar mass. Especially at the massive end scatter can influence the slope of the SMF, since there are few massive galaxies. This has an impact on γ and as all parameters are correlated scatter also affects the other parameters. We thus see a difference between the model without scatter and the most likely stellar mass in the model with scatter in Figure 6.

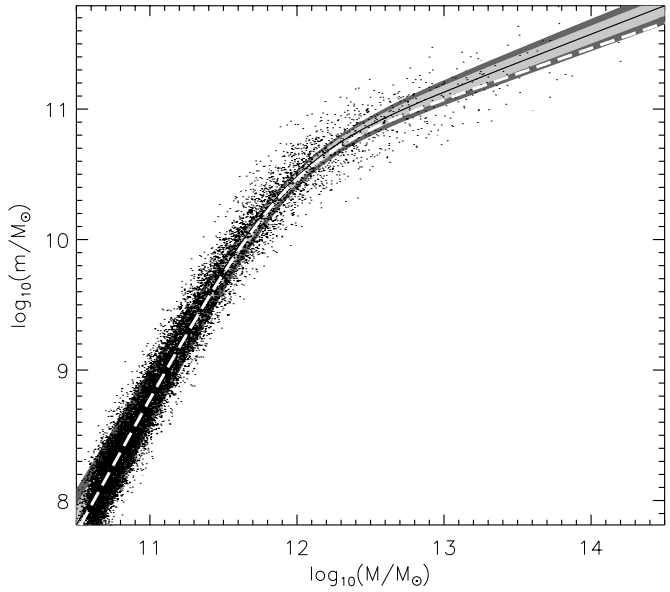

Figure 6. Stellar mass as a function of halo mass with $\sigma_m = 0.15$ dex. The solid line corresponds to our model without scatter, while the points represent the model with scatter (note that only 20% of the total number of objects are plotted). The relation between halo mass and the average stellar mass for the model with scatter is shown by the dashed line.

5. THE CONDITIONAL MASS FUNCTION

In the previous section, we derived a model that specifies the stellar mass of a central galaxy as a function of the virial mass of its host halo and the stellar mass of a satellite galaxy as a function of the maximum mass of the subhalo in which it lives. It has become common to represent the population of host halos by the HOD. This includes the halo occupation function $P(N|M)$ which is the probability distribution that a halo of mass M contains N galaxies (of a specific type). A close relative of the HOD is the "CLF" (e.g., Yang et al. 2003, 2004; van den Bosch et al. 2007). It extends the halo occupation function $P(N|M)$ (which gives only information about the total number of galaxies per halo in a given luminosity range) and yields the average number of galaxies with luminosities in the range $L \pm dL/2$ as a function of the virial mass M of their host halo.

We define its analog, the "conditional mass function" (CMF), or the average number of galaxies with stellar masses in the range $m \pm dm/2$ as a function of the virial mass M of their host halo. This provides a direct link between the SMF $\Phi(m)$ and the host halo mass function $dn(M)/dM$:

$$\Phi(m) = \int_0^\infty \Phi(m|M)\frac{dn(M)}{dM}dM. \quad (5)$$

A host halo of mass M can contain a whole population of galaxies with different stellar masses m. If we count the number of galaxies living in host halos with a virial mass in the range $M \in [M_1, M_2]$, we can compute the SMF of the halo bin $[M_1, M_2]$:

$$\tilde{\Phi}(m) = \int_{M_1}^{M_2} \Phi(m|M)\frac{dn(M)}{dM}dM \approx \Phi(m|\bar{M})\Delta n. \quad (6)$$

The tilde over a function represents the fact that it is computed in a halo mass bin. We have replaced the integral by a "tophat" with a width of Δn (number of host halos in the bin) and a height of $\Phi(m|M_m)$, where $\bar{M}$ is the geometric mean of the minimum and maximum halo masses bracketing the bin.

This equation allows us to put constraints on $\Phi(m|M)$ by calculating $\tilde{\Phi}(m)/\Delta n$. We can then choose an adequate parameterization of $\Phi(m|M)$ and fit these parameters to $\tilde{\Phi}(m)/\Delta n$ in every halo mass bin. Finally, we can investigate the halo mass dependence of the parameters.

5.1. Parameterization

In order to specify the CMF $\Phi(m|M)$, we divide the galaxy population into a central and a satellite part, as in the updated CLF formalism (Zheng et al. 2005; Zehavi et al. 2005; Cooray 2006; Yang et al. 2008; Cacciato et al. 2009). The central part is $\Phi_c(m|M)$ and the satellite part is $\Phi_s(m|M)$. Then the total CMF is the sum of both parts:

$$\Phi(m|M) = \Phi_c(m|M) + \Phi_s(m|M). \quad (7)$$

Note that both $\Phi_c(m|M)$ and $\Phi_s(m|M)$ are statistical functions and should not be regarded as the mass functions of galaxies living in a given individual halo.

For the central population, we expect the CMF to have a peak around the stellar mass m_c that corresponds to the host halo's virial mass M in the SHM relation (Equation 2). Due to the halo mass bin size this distribution gets smeared out, because halos in the interval $[M_1, M_2]$ contain central galaxies of stellar masses $m \in [m_1(M_1), m_2(M_2)]$. Thus, $\tilde{\Phi}(m)/\Delta n$ will be finite inside the interval $[m_1(M_1), m_2(M_2)]$ and zero elsewhere with a normalization such that the number of central galaxies per halo equals one. This can be regarded as scatter $\sigma_{\rm bin}$ due to the binning. If we add intrinsic scatter σ_m to Equation (2), we expect $\Phi_c(m|M)$ to be a lognormal with a maximum around $m_c(M)$ and a variance of σ_m^2. To this scatter, the binning scatter $\sigma_{\rm bin}$ adds in quadrature (assuming that $\sigma_{\rm bin}$ and σ_m are uncorrelated), resulting in a total scatter of $\sigma_c^2 = \sigma_m^2 + \sigma_{\rm bin}^2$. For both cases ($\sigma_m = 0$ and $\sigma_m \neq 0$), we use a lognormal distribution:

$$\Phi_c(m|M) = \frac{1}{\sqrt{2\pi}\ln 10\, m\, \sigma_c}\exp\left[-\frac{\log^2(m/m_c)}{2\sigma_c^2}\right], \quad (8)$$

where the mean $m_c(M)$ and width $\sigma_c^2(M)$ are parameterized functions of the halo mass M.

For the satellite population, we adopt a Schechter function with a steeper slope for the massive end. This is done by squaring the argument of the exponential function in the Schechter function:

$$\Phi_s(m|M) = \frac{\Phi_s^*}{m_s}\left(\frac{m}{m_s}\right)^{\alpha_s}\exp\left[-\left(\frac{m}{m_s}\right)^2\right]. \quad (9)$$

Also here the parameters $\Phi_s^*(M)$, $m_s(M)$, and $\alpha_s(M)$ are functions of the host halo mass M. They are the normalization, the characteristic mass, and the low-mass slope of the satellite population of host halos of mass M.

5.2. Constraining the Conditional Mass Function

We populate the halos and subhalos in our simulation with central and satellite galaxies according to the prescription in Section 3. Then we choose halo mass bins between $\log M/M_\odot = 10.2$ and $\log M/M_\odot = 15.0$ with a bin size of $\Delta M = 0.4$ dex. In every halo mass bin, we seek all galaxies which live in a host halo with a mass in that bin, which we divide between central and satellite galaxies. For these populations, we then compute two separate SMFs which we normalize such that

the number of central galaxies per host halo equals one. This procedure then yields for every halo mass bin a central and a satellite distribution $(d\tilde{n}_g/d\log M)\Delta n_h$.

Using Equation (6), we can now relate the SMF in a halo mass bin to the CMF:

$$\frac{d\tilde{n}_g(m)}{d\log M}\frac{1}{\Delta n_h} = \frac{\ln 10}{\Delta n_h} M \frac{d\tilde{n}_g(m)}{dM} = \ln 10\, M \frac{\tilde{\Phi}(m)}{\Delta n_h} \approx \ln 10\, M\, \Phi(m|M). \quad (10)$$

Now we can fit the five parameters $m_c(M)$, $\sigma_c(M)$, $m_s(M)$, $\Phi_s^*(M)$, and $\alpha_s(M)$ to the SMFs in each halo bin. We compute and fit the central and the satellite parts separately.

The left panels of Figure 7 show the CMF in a subsample of halo mass bins running from $\log M/M_\odot = 10.2\pm0.2$ to 15.0 ± 0.2, where we have not included intrinsic scatter in the SHM relation. For the satellite part, only galaxies with a mass above the completeness limits for each halo mass bin (as indicated in Figure 7) have been used in the fit.

In low-mass halos ($\log M/M_\odot < 11.0$), the contribution from satellite galaxies is very small and the central contribution dominates until $\log M/M_\odot = 12.0$. For massive halos ($\log M/M_\odot > 13.0$), the satellite contribution dominates by number. The mean of the lognormal fit to the central contribution also increases with halo mass as stipulated by the model derived in Section 3. The characteristic mass scale of the satellite contribution also increases with halo mass meaning that the most massive satellite galaxies have a mass which is comparable to the mass of the central galaxy.

The scatter of the central contribution $\sigma_c(M)$ decreases with halo mass. As we did not include any scatter in the model, this scatter reflects the width (0.4 dex) of the halo mass bins ($\sigma_{\rm bin}$). The halo mass dependence of $\sigma_c(M)$ arises because a fixed halo mass bin is mapped to a smaller galaxy mass bin for larger halo mass due to the shape of the SHM relation. Another feature of the CMF is the slope for low mass satellite galaxies $\alpha_s(M)$ which becomes shallower with increasing halo mass.

5.3. The Parameters of the Conditional Mass Function

In this section, we investigate the halo mass dependence of the five parameters of the CMF: $m_c(M)$, $\sigma_c(M)$, $m_s(M)$, $\Phi_s^*(M)$, and $\alpha_s(M)$. They have been fixed by fitting to the SMFs in each halo mass bin. We introduce a parameterization in order to describe the dependence on halo mass and constrain these by a fit to each parameter. The results are presented in Table 3. This provides a complete description of the CMF.

As we have already determined the mean relation between the stellar mass of a galaxy and the mass of its halo, the form of $m_c(M)$ has to be the same and can thus be described by Equation (2):

$$m_c(M) = 2\, M \left(\frac{m_c}{M}\right)_0 \left[\left(\frac{M}{M_{1c}}\right)^{-\beta_c} + \left(\frac{M}{M_{1c}}\right)^{\gamma_c}\right]^{-1}. \quad (11)$$

This yields four parameters $(m_c/M)_0$, M_{1c}, β_c, and γ_c.

In the upper left panel of Figure 8, $m_c(M)$ is plotted as a function of halo mass. Note that by construction, it has the same form as the SHM relation.

The scatter of the central galaxy contribution is high for low halo masses and decreases for more massive halos. The middle left panel of Figure 8 shows $\sigma_c(M)$ as a function of halo mass. As one can see, $\sigma_c(M)$ goes to a constant value both for low and high halo masses while it decreases with halo mass. We therefore choose the following parameterization:

$$\sigma_c(M) = \sigma_\infty + \sigma_1 \left[1 - \frac{2}{\pi}\arctan\left(\xi \log \frac{M}{M_2}\right)\right]. \quad (12)$$

This yields four more parameters σ_∞, σ_1, ξ, and M_2. Here, σ_∞ sets the high mass limit of $\sigma_c(M)$ while σ_1 sets the difference between the low and high mass limits of $\sigma_c(M)$. The parameter M_2 determines the mass scale at which the transition occurs and ξ sets the strength. For a large (small) value of ξ, the transition occurs in a small (large) interval around M_2.

The specific shape of $\sigma_c(M)$ can be explained by the form of the SHM relation (Equation (2)). As we have not included any scatter in this relation ($\sigma_m = 0$), the width of the lognormal function of the central galaxy distribution arises from the width of the halo mass bin ($\sigma_c = \sigma_{\rm bin}$). A halo mass interval $[M_1, M_2]$ contains only central galaxies with stellar masses of $m \in [m_1(M_1), m_2(M_2)]$. The lower left panel of Figure 8 illustrates this by showing how halo mass bins affect the bin size of the stellar mass. If we choose the same bin size for low and high mass halos, we get different bin sizes for low and high mass galaxies, due to the changing slope of $m(M)$. Therefore, the transition occurs where the slope of $m(M)$ changes which is around M_1, so the value of M_2 is very close to that value.

As Figure 7 shows that the satellite contribution falls off around the mean mass of the central galaxy, we expect the characteristic mass of the modified Schechter function $m_s(M)$ to follow $m_c(M)$. We therefore describe $m_s(M)$ with the same function we used for the parameterization of $m_c(M)$:

$$m_s(M) = 2\, M \left(\frac{m_s}{M}\right)_0 \left[\left(\frac{M}{M_{1s}}\right)^{-\beta_s} + \left(\frac{M}{M_{1s}}\right)^{\gamma_s}\right]^{-1}. \quad (13)$$

This function yields four parameters $(m_s/M)_0$, M_{1s}, β_s, and γ_s.

Table 3
Parameters of the CMF

Parameter	$\sigma_m = 0.0$		$\sigma_m = 0.15$	
$\log M_{1c}$	11.9347	$\pm$ 0.0257	11.9008	$\pm$ 0.0119
$(m_c/M)_0$	0.0267	$\pm$ 0.0006	0.0297	$\pm$ 0.0004
β_c	1.0059	$\pm$ 0.0332	1.0757	$\pm$ 0.0097
γ_c	0.5611	$\pm$ 0.0065	0.6310	$\pm$ 0.0121
$\log M_2$	11.9652	$\pm$ 0.1118	11.8045	$\pm$ 0.0458
σ_∞	0.0569	$\pm$ 0.0052	0.1592	$\pm$ 0.0030
σ_1	0.1204	$\pm$ 0.0191	0.0460	$\pm$ 0.0029
ξ	6.3020	$\pm$ 3.0720	4.2503	$\pm$ 0.9945
$\log M_{1s}$	12.1988	$\pm$ 0.0878	12.0640	$\pm$ 0.0931
$(m_s/M)_0$	0.0186	$\pm$ 0.0012	0.0198	$\pm$ 0.0015
β_s	0.7817	$\pm$ 0.0629	0.8097	$\pm$ 0.0971
γ_s	0.7334	$\pm$ 0.0452	0.6910	$\pm$ 0.0390
$-\log \Phi_0$	11.1622	$\pm$ 0.2874	10.8924	$\pm$ 0.4615
λ	0.8285	$\pm$ 0.0215	0.8032	$\pm$ 0.0367
$\log M_3$	12.5730	$\pm$ 0.1351	12.3646	$\pm$ 0.0260
$-\alpha_\infty$	1.3740	$\pm$ 0.0066	1.3676	$\pm$ 0.0043
$-\alpha_1$	0.0309	$\pm$ 0.0076	0.0524	$\pm$ 0.0051
ζ	4.3629	$\pm$ 2.6810	9.5727	$\pm$ 6.8240

Notes. The second and third columns give the CMF parameters and their errors for a model without scatter while the fourth and the fifth columns give the CMF parameters and their errors for a model with a scatter of $\sigma_m = 0.15$. All quoted masses are in units of $M_\odot$.

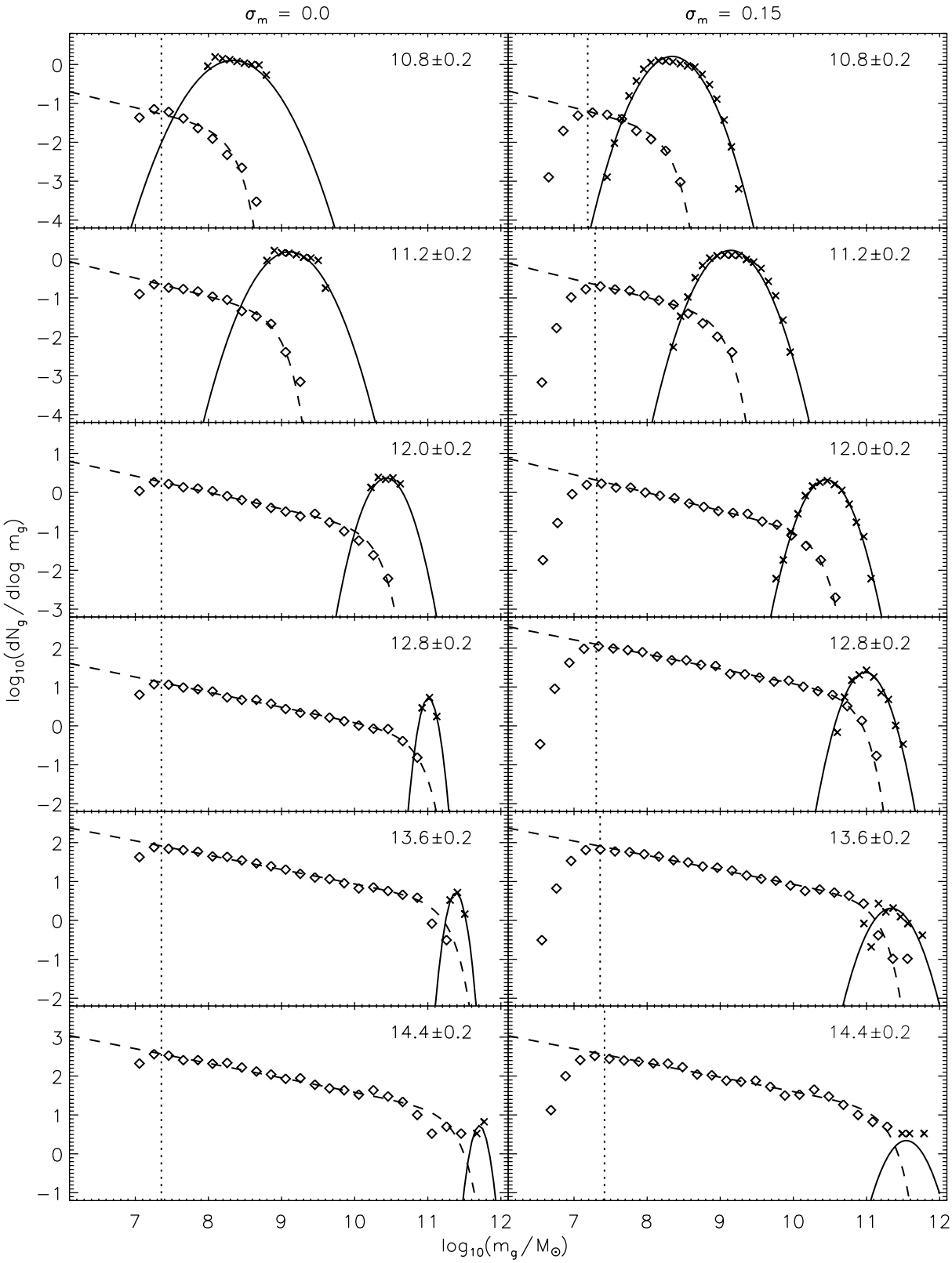

Figure 7. Conditional mass function (CMF) predicted by our model at $z = 0$. We plot the derived SMFs ($d\tilde{n}_g/d \log m$) in a subsample of halo mass bins. The left panels show the CMF for a model without scatter, while the right panels show the CMF with scatter of $\sigma_m = 0.15$. The label in each panel is the range of host halo mass $\log M/M_\odot$. The stellar mass functions are normalized such that a host halo contains exactly one central galaxy. The total CMF consists of a central galaxy part (crosses) and a satellite part (diamonds). The central part is described by a lognormal distribution (solid line) and the satellite part is described by a truncated Schechter function (dashed line) using the parameters that were derived by a fit to the CMF. The dotted line shows the completeness limit used in the fit to the satellite contribution.

The upper right panel of Figure 8 plots $m_s(M)$ as a function of halo mass. We see that the shape is similar to that of $m_c(M)$. Note that $m_s(M)$ is always lower than $m_c(M)$, while the deviation increases with increasing halo mass. This implies that for high

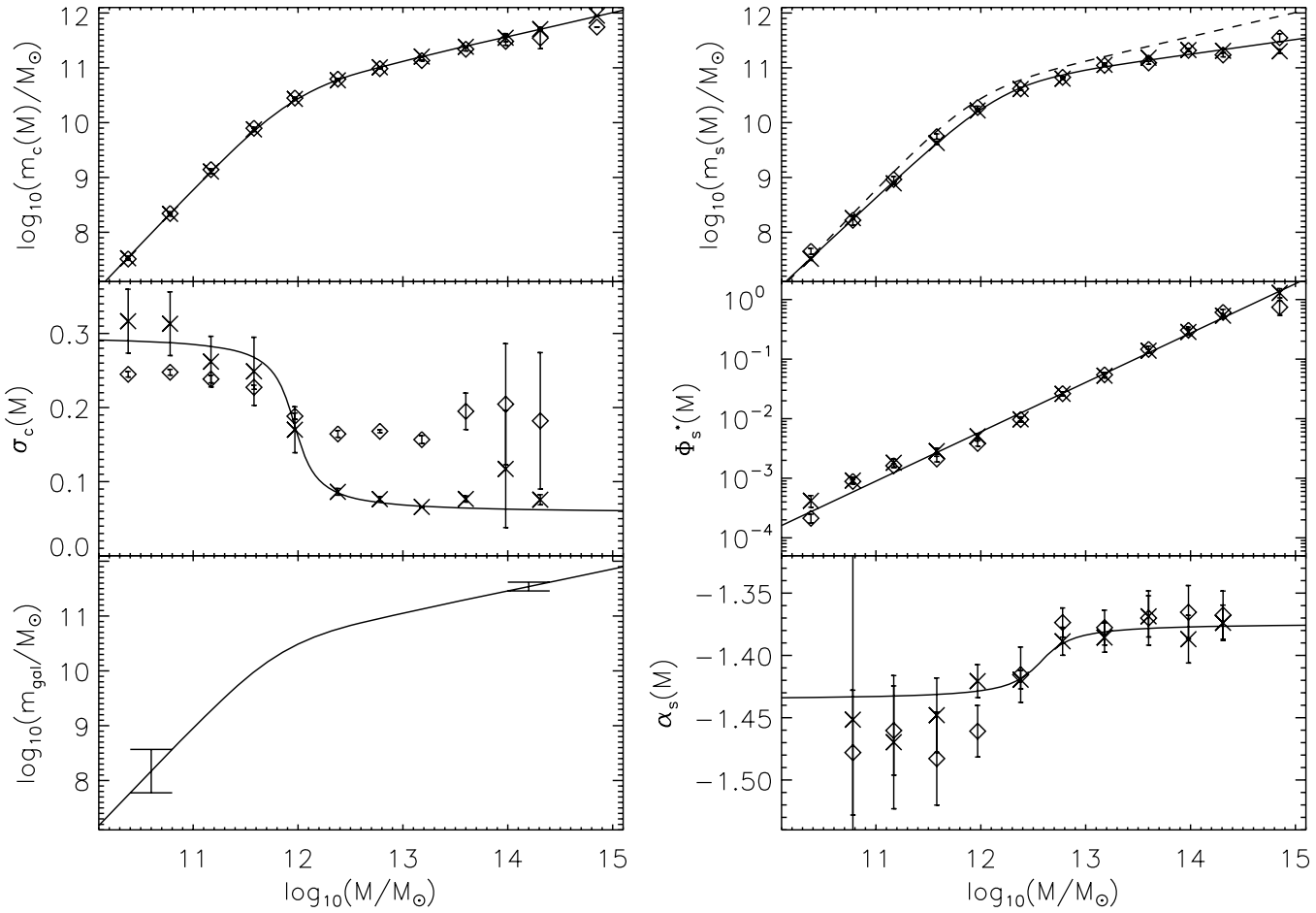

Figure 8. Five parameters of the conditional mass function as a function of halo mass. The crosses were derived from a fit to the CMF in every halo mass bin (assuming no scatter in stellar-to-halo mass relation). The solid line is a fit to the crosses using the respective parameterization. The CMF parameters derived with a scatter of $\sigma_m = 0.15$ in the stellar-to-halo mass relation are given by the diamonds. The left panels show the central contribution: $m_c(M)$ (top panel), $\sigma_c(M)$ (middle panel), and an illustration of the behavior of $\sigma_c(M)$ (bottom panel). The right panels show the satellite contribution: $m_s(M)$ (top panel), $\Phi_s^*(M)$ (middle panel), and $\alpha_s(M)$ (bottom panel). The dashed line in the top right panel indicating $m_c(M)$ has been added for comparison.

halo masses the satellite contribution to the CMF falls off before the mean mass of the central galaxy.

The normalization of the modified Schechter function is small for low halo masses and increases with the mass of the host halo. The middle right panel of Figure 8 shows $\Phi_s^*(M)$ as a function of halo mass. We see that $\Phi_s^*(M)$ can be described by a power law and choose the following parameterization:

$$\Phi_s^*(M) = \Phi_0 \left(\frac{M}{M_\odot}\right)^{\lambda}. \quad (14)$$

We get two more parameters, Φ_0 and λ. The normalization of $\Phi_s^*(M)$ is given by Φ_0 and the slope by λ. The shape of $\Phi_s^*(M)$ implies that the probability for a host halo to harbor satellite galaxies (in a given stellar mass range) increases with increasing halo mass.

The slope of the modified Schechter function for the satellite contribution becomes shallower for more massive halos. The lower right panel of Figure 8 shows $\alpha_s(M)$ as a function of halo mass and shows that $\alpha_s(M)$ goes to a constant value for both low and high halo masses. Similar to $\sigma_c(M)$, we choose the parameterization:

$$\alpha_s(M) = \alpha_\infty + \alpha_1 \left[1 - \frac{2}{\pi} \arctan\left(\zeta \log \frac{M}{M_3}\right)\right]. \quad (15)$$

This yields four more parameters α_∞, α_1, ζ, and M_3. Here, α_∞ sets the high mass limit of $\alpha_c(M)$ while α_1 sets the difference between the low and high mass limits of $\alpha_c(M)$. The mass scale at which this transition occurs is determined by M_3 and ζ sets its strength. The transition occurs in a small (large) interval around M_3 for a large (small) value of ζ.

5.4. The Impact of Scatter

Until now, we have used the SHM Equation (2) without any intrinsic scatter. In this section, we investigate how the CMF and the parameters change if we include a scatter σ_m as described in Section 4.5. This scatter is again assumed to be constant with host halo mass.

The right panels of Figure 7 show the resulting CMF in a subsample of halo mass bins for an intrinsic scatter of $\sigma_m = 0.15$. The central part is now no longer near-constant in the interval $[m(M - \Delta M/2), m(M + \Delta M/2)]$ as in the left panels of Figure 7 (where $\sigma_m = 0.0$) but has the form of a lognormal with a broader distribution for bigger σ_m. As the scatter has been taken from a lognormal distribution, the central galaxy contribution to the CMF is distributed in the same way. Hence, $\sigma_c(M)$ changes with respect to the model that does not include artificial scatter. We notice that at the massive end the binning scatter $\sigma^2_{\rm bin}$ and the intrinsic scatter σ^2_m add to the total scatter $\sigma^2_{\rm tot}$. At the low mass end, however, the total scatter is less

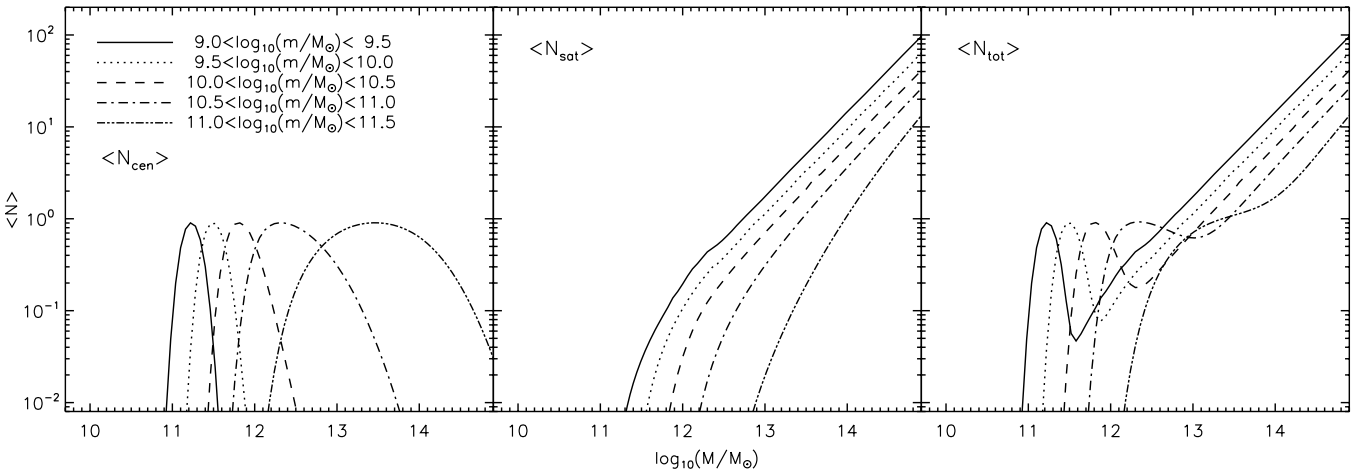

Figure 9. Occupation numbers as function of halo mass in stellar mass bins, derived using the conditional mass function. The left, middle, and right panels show the average number of central, satellite, and total galaxies per halo, respectively.

than what has been obtained by using no intrinsic scatter. This shows that the two forms of scatter do not add in quadrature and indicates that they are correlated.

We compare $m_c(M)$, $\sigma_c(M)$, $m_s(M)$, $\Phi_s^*(M)$, and $\alpha_s(M)$ for $\sigma_m = 0$ and $\sigma_m = 0.15$ and show the resulting parameters in Table 3 (Columns 4 and 5) and in Figure 8. The mean mass of the central galaxy $m_c(M)$ does not change much if artificial scatter is introduced. The most likely stellar mass of a central galaxy is still given by the SHM relation, so the mean of the Gaussian in logarithmic space stays the same. Also the parameters of the satellite population ($m_s(M)$,$\Phi_s^*(M)$, and $\alpha_s(M)$) do not change significantly.

5.5. The Occupation Numbers

In order to compare our results to other HOD models, it is useful to compute the average number of galaxies per halo $\langle N\rangle$, as this is the main prediction of the HOD approach. To compute $\langle N\rangle(M)$ from the CMF, we simply integrate $\Phi(m|M)$ over the desired stellar mass range:

$$\langle N\rangle(M) = \int_{m_1}^{m_2} \Phi(m|M)dm. \tag{16}$$

As we have divided $\Phi(m|M)$ into a central galaxy contribution $\Phi_c(m|M)$ and a satellite galaxy contribution $\Phi_s(m|M)$, we can compute separate occupation numbers for central and satellite galaxies:

$$\begin{aligned}\langle N\rangle(M) &= \int_{m_1}^{m_2} \Phi_c(m|M)dm + \int_{m_1}^{m_2} \Phi_s(m|M)dm \\ &= \langle N_c\rangle(M) + \langle N_s\rangle(M).\end{aligned}$$

The average number of central galaxies per halo $\langle N_c\rangle(M)$ is given by

$$\langle N_c\rangle(M) = \tfrac{1}{2}\left[\mathrm{erf}(\eta_2) - \mathrm{erf}(\eta_1)\right] , \tag{17}$$

with the error function $\mathrm{erf}(x)$ and the integration boundaries

$$\eta_1 = \frac{\log(m_1/m_c)}{\sqrt{2}\sigma_c} \quad \text{and} \quad \eta_2 = \frac{\log(m_2/m_c)}{\sqrt{2}\sigma_c} .$$

The average number of satellite galaxies per halo $\langle N_s\rangle(M)$ is

$$\langle N_s\rangle(M) = \frac{\Phi_s}{2}\left[\Gamma\left(\frac{\alpha_s}{2}+\frac{1}{2},\kappa_1\right) - \Gamma\left(\frac{\alpha_s}{2}+\frac{1}{2},\kappa_2\right)\right] , \tag{18}$$

with the upper incomplete gamma function $\Gamma(a, x)$ and the integration boundaries

$$\kappa_1 = (m_1/m_s)^2 \quad \text{and} \quad \kappa_2 = (m_2/m_s)^2 .$$

Figure 9 shows the resulting occupation numbers for the values of the CMF parameters that were derived in Section 5.3 (using a scatter of $\sigma_m = 0.15$). The five lines in each panel correspond to different stellar mass bins.

The left panel shows the average number of central galaxies per halo $\langle N_c\rangle(M)$ as a function of halo mass. In the middle panel, the average number of satellite galaxies per halo $\langle N_s\rangle(M)$ as a function of halo mass is shown. The right panel plots the average number of all galaxies per halo $\langle N_{\rm tot}\rangle(M)$ as a function of halo mass. A galaxy of a low stellar mass can thus either be a central galaxy of a low-mass halo, or a satellite galaxy of a massive halo. It is not likely to live in a halo of intermediate mass.

As it is common in the literature to plot occupation numbers not for stellar mass intervals, but for galaxy samples with a mass above a given threshold, we need to adjust Equations (17) and (18). The stellar mass threshold is then given by m_1 while $m_2 \to \infty$. This yields for the average number of central galaxies

$$\langle N_c\rangle(M, m_1) = \frac{1}{2}\left[1 - \mathrm{erf}\left(\frac{\log(m_1/m_c)}{\sqrt{2}\sigma_c}\right)\right] , \tag{19}$$

since $\mathrm{erf}(x \to \infty) \to 1$, and for the average number of satellite galaxies

$$\langle N_s\rangle(M, m_1) = \frac{\Phi_s}{2}\,\Gamma\left[\frac{\alpha_s}{2}+\frac{1}{2},\left(\frac{m_1}{m_s}\right)^2\right], \tag{20}$$

since $\Gamma(a, x \to \infty) \to 0$.

Figure 10 shows occupation numbers for different stellar mass thresholds. The left panel shows the average number of central galaxies per halo $\langle N_c\rangle(M)$ as a function of halo mass. The middle panel plots the average number of satellite galaxies per halo $\langle N_s\rangle(M)$ as a function of halo mass. It is similar to the middle panel of Figure 9, while it is larger at a given halo mass. In the right panel, the average number of all galaxies per halo $\langle N_{\rm tot}\rangle(M)$ as a function of halo mass is shown.

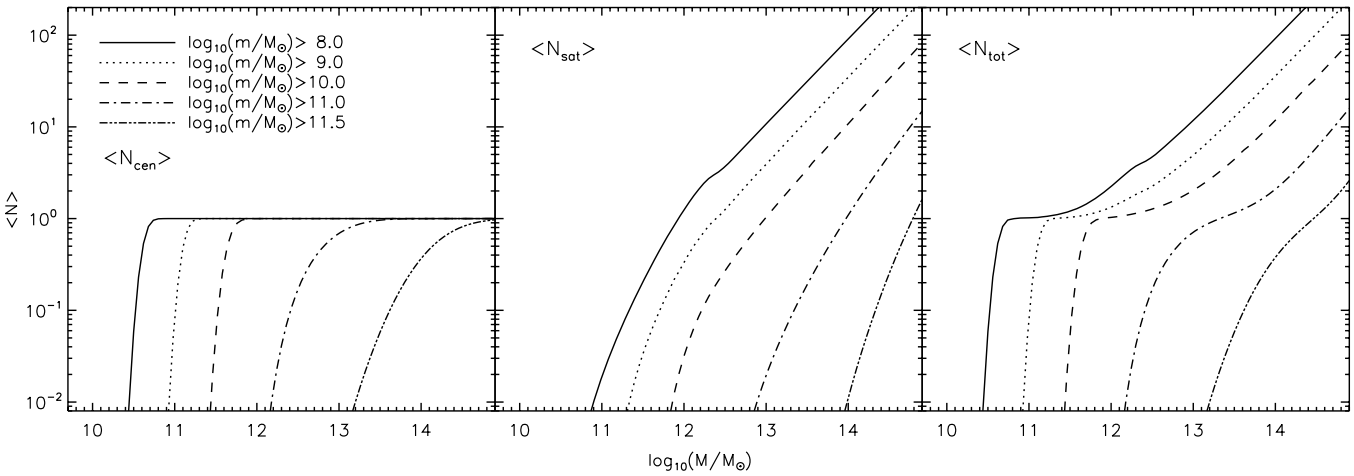

Figure 10. Occupation numbers as function of halo mass for galaxy samples with a stellar mass above a given threshold. The left, middle, and right panels show the average number of central, satellite, and total galaxies per halo, respectively.

Table 4
Comparison Between Different Models

Model	log M_1	$(m/M)_0$	β	γ
Our model	11.884	0.0282	1.06	0.556
Non-parametric	11.766	0.0324	1.43	0.565
Wang et al. (2006)	11.845	0.0319	1.42	0.710
Somerville SAM	11.888	0.0276	0.98	0.629
Croton SAM	11.742	0.0405	0.92	0.610
Yang GC	12.067	0.0384	0.71	0.698

Note. All quoted masses are in units of $M_\odot$.

6. COMPARISON

6.1. Other HOD Models

Numerous variations on halo occupation models have been presented in the literature. In this section, we describe some of the most popular ones and compare them to our model. As many authors use different IMFs and definitions of halo masses, we convert all results to the conventions that we have used in this work (Kroupa IMF and virial overdensity).

In the non-parametric model (Vale & Ostriker 2006; Conroy et al. 2006; Shankar et al. 2006), galaxy properties, such as luminosity and stellar mass, are monotonically related to the mass of dark matter halos. Using the observed galaxy SMF, the most massive halo is matched to the most massive galaxy:

$$n_g(> m_i) = n_h(> M_i). \quad (21)$$

In this way, the observed SMF is automatically reproduced. Applying this procedure and fitting the parameters of the SHM relation to the result, we have derived the values given in Table 4. These are in good agreement with the parameters of our model, except for β. We find that this is due to the shape of the SHM ratio for low masses. For the non-parametric model, $m(M < M_1)$ cannot be perfectly described by a single power law, as is assumed in our model.

Adding an additional parameter and assuming a fitting function with five free parameters, we are able to fit the SHM relation predicted by the non-parametric model quite precisely. The fifth parameter accounts for the deviation from the power law at high and low masses. Using the parameterization

$$m(M) = m_0 \frac{(M/M_1)^{\gamma_1}}{\left[1 + (M/M_1)^{\beta}\right]^{(\gamma_1-\gamma_2)/\beta}}, \quad (22)$$

we determine the values given in Table 5. Figure 11 shows the results of four- and five-parameter fits to the SHM relation derived via the non-parametric method, compared with our usual model. In the range where we applied the mass function fit, the non-parametric model lies within our error bars.

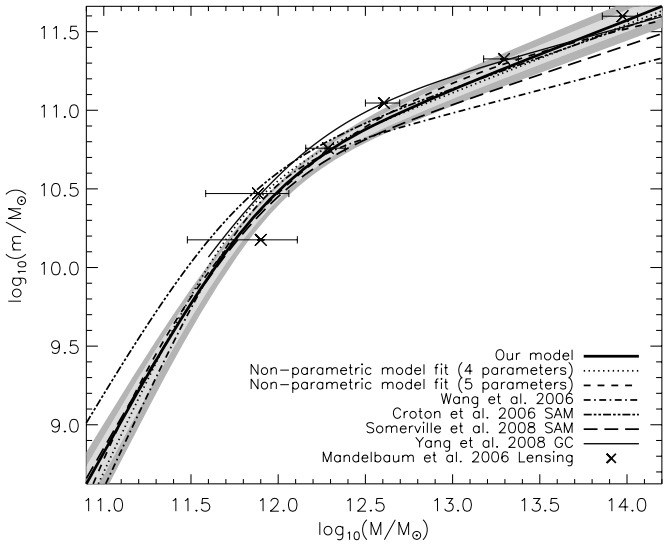

Figure 11. Comparison of the stellar-to-halo mass relation $m(M)$ between our model (solid line), models from other authors and galaxy–galaxy lensing (symbols). The blue areas are the 1σ and 2σ levels and the error bars on the symbols are the 2σ levels of the halo mass.

Table 5
Fit Parameters for Equation (22)

log m_0	log M_1	γ_1	γ_2	β
10.864	10.456	7.17	0.201	0.557
±0.043	±0.211	±1.16	±0.018	±0.031

Note. All masses are in units of $M_\odot$.

In Wang et al. (2006), a model similar to ours is used to constrain the SHM ratio. The halo catalog is taken from the Millennium simulation (Springel et al. 2005); halos are identified using a FoF group finder while substructure is found using the SUBFIND algorithm of Springel et al. (2001). As observational constraints, the authors use a SMF which they compute from the SDSS DR2 data using the mass estimates of Kauffmann et al. (2003) and the projected CFs of Li et al. (2006).

The parameterization they use is similar to ours, with four free parameters that can easily be converted to M_1, $(m/M)_0$, β, γ, and an unconstrained scatter. These are fixed by generating a grid of models and the best-fit model is defined as the one for which $\chi^2 = \chi^2(\Phi) + \chi^2(w_p)$ is minimal. They find that their fit improves if they take a different set of parameters for central and satellite galaxies. In Table 4, we compare our best-fit parameters with their central galaxy best-fit parameters which have been updated in Wang et al. (2007). We show these results in Figure 11.

The values of M_1 and $(m/M)_0$ are in very good agreement with our values, but the slopes are both higher, resulting in fewer massive and fewer low mass galaxies. The reason for the difference in the low mass end is the different simulation used. As the resolution of the simulation in our model is higher, the low mass end can be constrained more tightly. For the massive end, the difference in γ can be explained by the additional unconstrained scatter that is used in Wang et al. (2006). As the mass function is steep at high masses and shallow for low masses, a change in the scatter will influence the number of massive galaxies strongly, while it will have only a small effect on the low mass end. As the other three parameters, M_1, $(m/M)_0$, and β, are coupled to the Schechter function parameters, there are two parameters to constrain the slope of the massive end of the SMF. This degeneracy can cause the difference in γ between the two models. The fact that in the Millennium simulation the cosmology is different to that of our simulation also affects the value of the parameters.

6.2. Gravitational Lensing

The relation between stellar mass and halo mass can be observationally constrained using galaxy–galaxy lensing. Gravitational lensing induces shear distortions of background objects around foreground galaxies, allowing the mass of the dark matter halo to be estimated. Mandelbaum et al. (2005, 2006) have used SDSS data to calibrate the predicted signal from a halo model which has been derived from a dissipationless simulation. They have extracted the mean halo mass as a function of stellar mass. The lensing data for combined early- and late-type galaxies (R. Mandelbaum 2008, private communication) are shown in Figure 11 and are in excellent agreement with our model.

6.3. Semi-analytic Models

As we discussed in the introduction, SAMs of galaxy formation attempt to predict the relationship between dark halo mass and stellar mass by a priori modeling of physical processes, such as the growth of structure, cooling, star formation, and stellar and active galactic nucleus (AGN) feedback. We compare our results with predictions from the latest version of the SAMs of Somerville & Primack (1999); see Somerville et al. (2008). For this, we compute the mean stellar mass of central galaxies as a function of the mass of the host halo in halo mass bins. The results are shown in Figure 11 and are in good agreement with our model. This is not surprising, as the physical parameters in the model of Somerville et al. (2008) have been tuned to match the observed SMF at $z = 0$.

In Wang et al. (2006), the authors use the SAM of Croton et al. (2006) and link galaxy properties, such as the stellar mass, to the mass of the halo in which the galaxy was last a central object $M_{\rm infall}$. They fit the same four-parameter function that they used for their empirical model (described above) to obtain the parameter estimates from the SAM. We summarize these results in Table 4, and show them in Figure 11.

The two slopes are in very good agreement with our results. However, the normalization in the Croton et al. (2006) SAM is $\sim$25% higher and the characteristic mass is $\sim$25% lower than what we found and what Wang et al. (2006) found for their model. This is because the SAM of Croton et al. (2006) does not produce a perfect fit to the observed SMF.

6.4. SDSS Group Catalog

Another direct way of studying galaxy properties as a function of halo mass is using the SDSS group catalog presented in Yang et al. (2007). In this approach, galaxies are first linked together into "groups" using a FoF algorithm. Each group is then assigned a total halo mass by matching to the theoretical dark matter halo mass function. Yang et al. (2008) present the relation between the mean stellar mass of the central galaxy and the host halo mass. We fit the parameters of Equation (2) to their relation and present the results in Table 4.

We note that the characteristic mass and the normalization derived from the group catalog are both higher than our model parameters. The high-mass slope of the SHM relation in the group catalog is shallower than that of our model. The low-mass slope is also shallower, however, the constraints on the low-mass slope in the group catalog are weak, since the lowest halo masses are $\log(M/M_\odot) \sim 11.7$. This can also be seen in Figure 11 where we show the SHM relation of the group catalog for comparison.

7. HIGH REDSHIFT

The discussion in the previous sections has focussed solely on the present day universe. In this section, we extend our analysis to higher redshifts and derive the redshift dependence of the SHM relation. Having chosen a particular observed SMF at a given redshift, we can investigate how the parameters of the SHM ratio change with time. This allows us to learn about the evolution of galaxies. Also, with this information, we can populate the N-body simulation snapshots with galaxies at different redshifts using the appropriate redshift-dependent SHM relation, and then use the spatial information from the simulation to compute the stellar mass dependent correlation functions.

Since at the present time there are no high-redshift ($z \gtrsim 1$) clustering data as a function of stellar mass available, we fit the four parameters of Equation (2) to the observed SMFs at a given redshift. We argued in Section 4.2 that, under the assumption that central and satellite galaxies follow the same SHM relation, the SMFs provide much stronger constraints on the SHM ratio than the clustering data. Thus, we should be able to use our model to predict clustering as a function of stellar mass at any redshift.

7.1. Which Survey for Which Redshift

In order to constrain the SHM relation, we have to first select observational SMFs at the redshifts we want to investigate.

Because of the trade-off between surveying large areas and obtaining deep samples, measurements of the SMF at high redshift tend to suffer from limited dynamic range. Therefore, it is important to think about how the constraints on our four SHM function parameters arise from the observations.

The characteristic mass M_1 and the maximum SHM ratio $(m/M)_0$ mostly depend on galaxies and halos of intermediate mass. The high-mass slope γ is fixed by the number of massive galaxies since these live in the massive halos. On the other hand, the low-mass slope β is set by the number of low mass galaxies since these live in the low-mass halos.

For a survey with a fixed area on the sky, the observed volume is smaller for low redshifts ($z \lesssim 1$) than for high redshifts. In order to compute the SMF at high galaxy masses, the observed volume has to be relatively large, as massive galaxies are rare. Thus for low redshifts, one has to choose a wide survey (large area) to determine the SMF for massive galaxies and properly constrain γ. Constraining the SMF at the low mass end requires a high level of completeness for low mass galaxies, which are very faint objects. Hence, we have to choose a deep survey that can detect faint galaxies in order to constrain β.

Taking these considerations into account, we choose the SMFs presented in Drory et al. (2004) to constrain the parameters M_1, $(m/M)_0$, and γ at low redshifts. The authors derive the SMFs using MUNICS which is a wide area, medium-deep survey selected in the K band. The detection limit is $K \approx 19.5$ and the subsample the authors use covers 0.28 deg^2. We apply our method using these mass functions and take the three parameters from that analysis.

However, the MUNICS survey is not deep enough to detect galaxies that are fainter than the characteristic mass of the SMF (the knee) and thus is not sufficient to constrain the parameter β. To constrain β, we choose the SMFs derived in Fontana et al. (2006). This work is based on the GOODS-MUSIC sample, a multicolor catalog extracted from the survey conducted over the Chandra Deep Field South. The catalog is selected in the z_{850} and K bands, covers an area of 143.2 arcmin^2, and is complete to a typical magnitude of $K \approx 23.5$. We apply our method using the SMFs computed with the z_{850} band selected sample and take the parameter β from that analysis.

For high-redshift ($z \gtrsim 1$), we use the SMFs presented in Fontana et al. (2006) to constrain all four parameters. For high redshifts, the volume of a redshift bin becomes large enough to sample massive galaxies, and therefore the GOODS-MUSIC sample is sufficient to constrain γ.

We convert all SMFs which use a Salpeter IMF to the Kroupa/Chabrier IMF.

7.2. Evolution of the Parameters

Having selected the observational SMFs for a set of different redshifts, we fit the four free parameters M_1, $(m/M)_0$, β, and γ to the observations. The errors on the parameters are derived in a similar way as explained in Section 3.3, but instead of using confidence intervals we have fitted a Gaussian to the probability distributions of M_1, $(m/M)_0$, and γ and a lognormal to the probability distribution of β.

Figure 12 shows the observed and the model SMFs for different redshifts (indicated at the top of each panel). The values of the resulting four parameters for the different redshifts are shown in Table 6 and the redshift evolution is plotted in Figure 13. The characteristic mass M_1 grows with increasing redshift, while the normalization of the SHM ratio $(m/M)_0$ becomes smaller with increasing redshift. This means that there is less stellar content in a halo of a given mass at a higher redshift.

Table 6
Stellar-to-halo Mass Ratio Parameters for Different Redshifts

z	log M_1	$\pm$	$(m/M)_0$	$\pm$	β	$-$	$+$	γ	$\pm$
0.0	11.88	0.02	0.0282	0.0005	1.06	0.05	0.05	0.56	0.00
0.5	11.95	0.24	0.0254	0.0047	1.37	0.22	0.27	0.55	0.17
0.7	11.93	0.23	0.0215	0.0048	1.18	0.23	0.28	0.48	0.16
0.9	11.98	0.24	0.0142	0.0034	0.91	0.16	0.19	0.43	0.12
1.1	12.05	0.18	0.0175	0.0060	1.66	0.26	0.31	0.52	0.40
1.5	12.15	0.30	0.0110	0.0044	1.29	0.25	0.32	0.41	0.41
1.8	12.28	0.27	0.0116	0.0051	1.53	0.33	0.41	0.41	0.41
2.5	12.22	0.38	0.0130	0.0037	0.90	0.20	0.24	0.30	0.30
3.5	12.21	0.19	0.0101	0.0020	0.82	0.72	1.16	0.46	0.21

Notes. For M_1, $(m/M)_0$, and γ the errors are drawn from a Gaussian and thus are symmetric (indicated by the symbol $\pm$). For β, the errors are drawn from a lognormal distribution and thus there is a lower error (indicated by the symbol $-$) and an upper error (indicated by the symbol +). All quoted masses are in units of $M_\odot$.

The high-mass slope γ can be constrained only weakly. This is due to the limitation of the available galaxy surveys. As the area of the survey is small, the volume in which galaxies are detected is limited, and thus massive galaxies are very rare. This results in large error bars for the SMF for massive galaxies which propagate into the error bars of γ. The situation improves slightly for higher redshifts as the volume of higher redshift bins is larger and thus more massive galaxies can be observed. The value of γ decreases with increasing redshift. For higher redshifts ($z > 1$), the error bars on γ become very large because of the limited area covered by the available deep surveys (in this case, GOODS). We leave it up to the reader to assess the reliability of our results at $z > 1$ based on our quoted error bars.

The low-mass slope β seems to increase with redshift until $z \approx 2$ and then drops to a low value. However, as the redshift increases it becomes more and more difficult to observe low mass galaxies which are very faint. Thus, the high-redshift values for β are not very well constrained and perhaps not to be fully trusted. We therefore assume that β grows with increasing redshift.

As we explained in Section 4.4, β is strongly related to the parameter α of the Schechter function. A small value of β corresponds to a large absolute value of α, while a large value of β results in a low absolute value of α. This would mean that for higher redshifts the SMF would become shallower, in contradiction with observations (e.g., Fontana et al. 2006 show that the absolute value of α increases with redshift). However, one has to remember that the halo mass function also changes with redshift and becomes steeper. Thus, the halo mass function steepens more than the SMF, so β has to increase in order to compensate.

With the derived parameter values, it becomes possible to interpolate and find the SHM ratio at any redshift. This is done by choosing a redshift parameterization for each of the parameters.

As M_1 and $(m/M)_0$ do not change much above a redshift of $z > 1.5$, we choose power laws for the redshift dependence:

$$\log M_1(z) = \log M_1|_{z=0} \cdot (z+1)^{\mu} \tag{23}$$

and

$$\left(\frac{m}{M}\right)_0(z) = \left(\frac{m}{M}\right)_{z=0} \cdot (z+1)^{\nu} \tag{24}$$

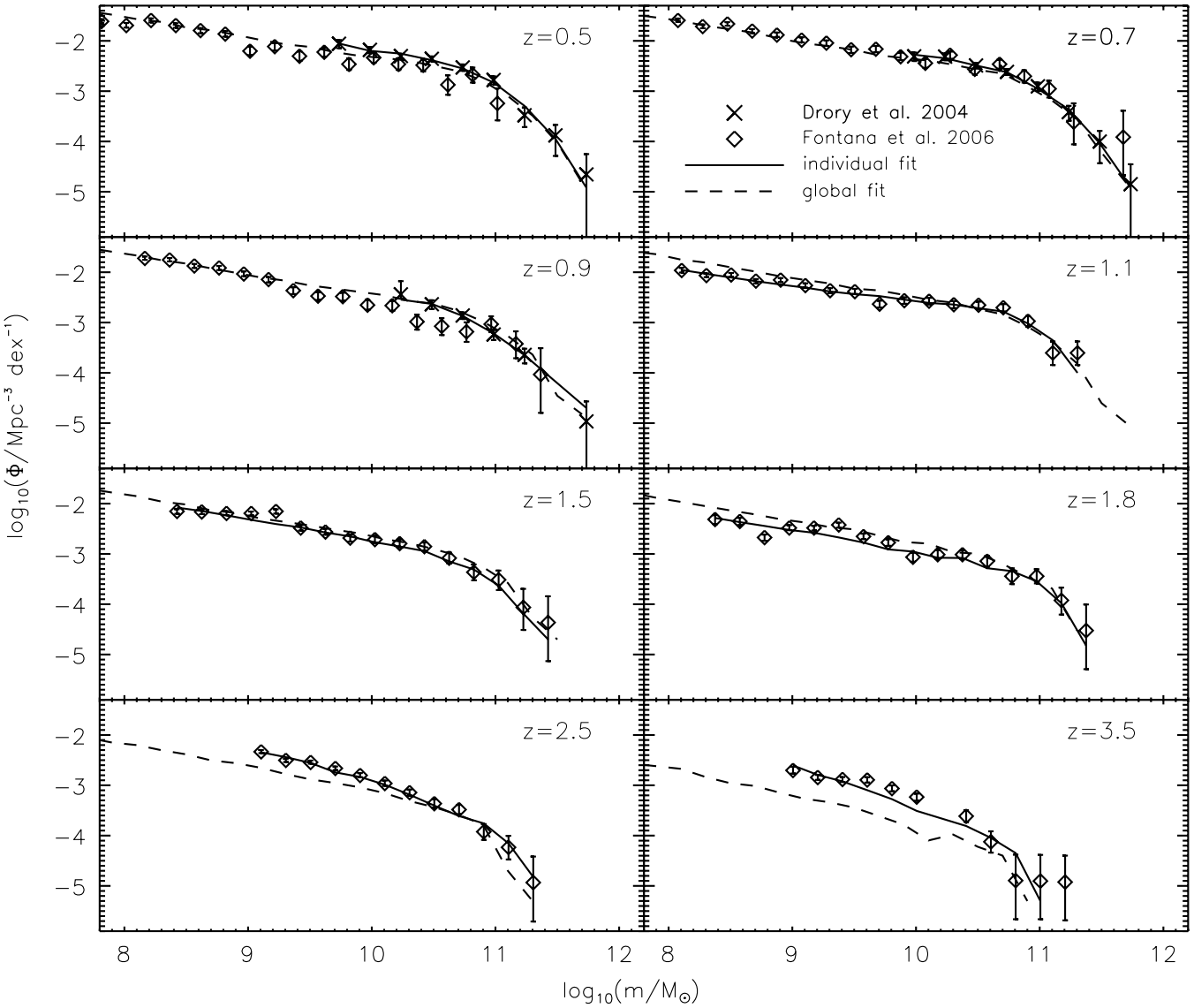

Figure 12. Comparison between the model and the observed stellar mass functions for different redshifts. The observed stellar mass functions are taken from Drory et al. (2004; for $z \leqslant 0.9$) and Fontana et al. (2006; for $z \geqslant 1.1$) and are represented by the symbols. The model stellar mass functions have been fitted to the observations and are represented by the solid lines. The dashed lines are the theoretical mass function we obtain from the redshift-dependent parameterization. The redshift is indicated at the top of each panel.

with the normalizations M_0 and $(m/M)_{z=0}$ and the slopes μ and ν.

To parameterize γ over redshift, a linear dependence would lead to a negative γ at a certain redshift. Though this is not forbidden, it leads to a SHM ratio which would be increasing monotonically with halo mass which is inconsistent with feedback processes at the massive end. Hence, we also choose a power-law parameterization for γ:

$$\gamma(z) = \gamma_0 \cdot (z+1)^{\gamma_1} \tag{25}$$

with the normalization γ_0 and the slope γ_1.

From Figure 13, we are not able to infer whether β converges to a constant value. Thus, we adopt a simple linear parameterization:

$$\beta(z) = \beta_1 \cdot z + \beta_0 \ . \tag{26}$$

Note that we have also tried other parameterizations (constant β, decreasing β) but could not reproduce the observed SMFs. Using the linear parameterization for β and the power laws for the other parameters, we were able to compute SMFs that are in good agreement with the observed ones.

Table 7
Parameters for Redshift-dependent Stellar-to-halo Mass Relation

$M_1\|_{z=0}$	μ	$(m/M)_{z=0}$	ν	γ_0	γ_1	β_0	β_1
11.88	0.019	0.0282	−0.72	0.556	−0.26	1.06	0.17
±0.01	±0.002	±0.0003	±0.06	±0.001	±0.05	±0.06	±0.12

Note. All quoted masses are in units of $M_\odot$.

A fit to the derived values presented in Table 6 yields the parameters given in Table 7. As we do not fully trust the derived values of β for $z \gtrsim 2$, we neglect these two values and fit a line to the remaining values of β.

7.3. The Stellar-to-halo Mass Relation for Different Redshifts

Having developed a redshift-dependent model of the SHM relation, we now test this model by computing interpolated SMFs for different redshifts. For this, we use the method described in Section 3. However, now we do not use the

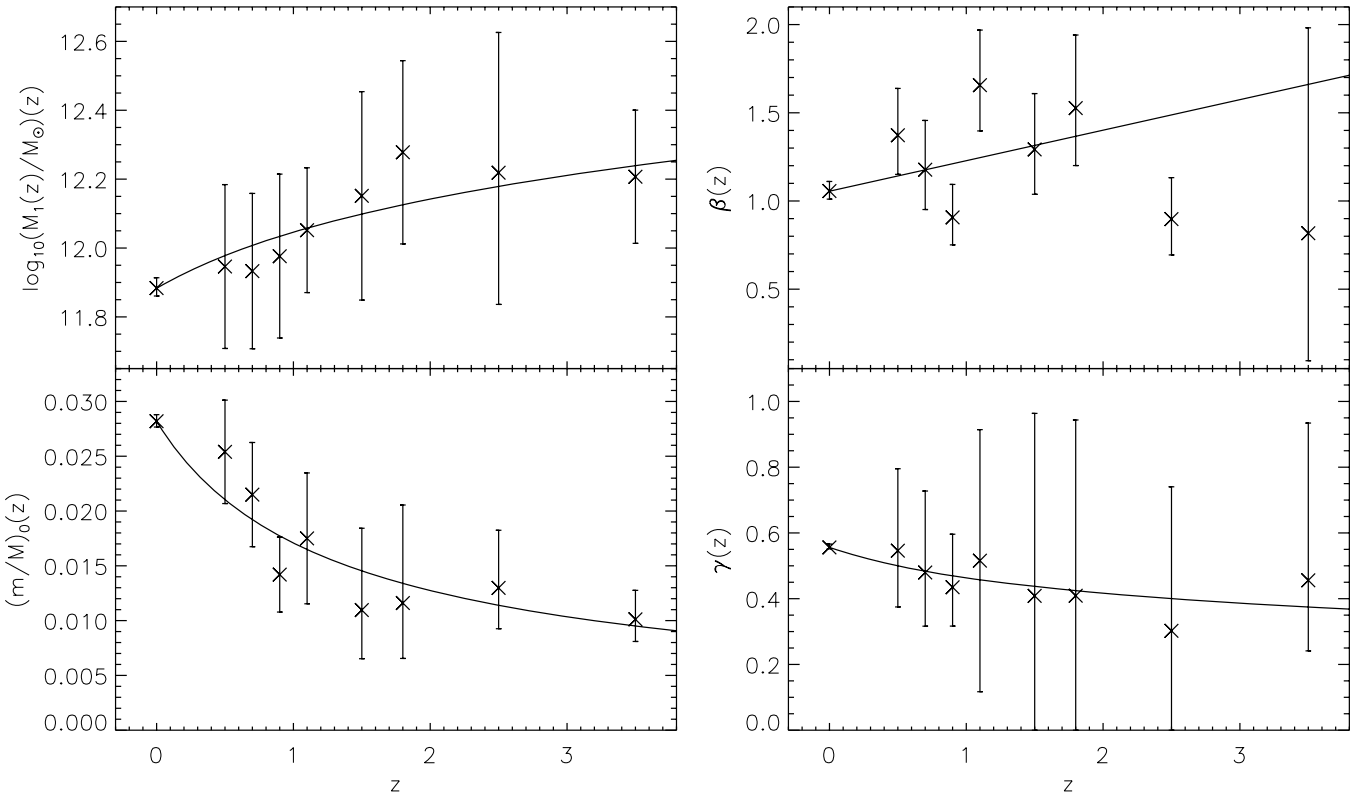

Figure 13. Evolution of the stellar-to-halo mass relation parameters with redshift. The symbols correspond to the derived values while the solid line is a fit to the data. For M_1, $(m/M)_0$, and γ this is a power law, while for β it is a straight line.

parameters that have been derived at each redshift by fitting the model to the observations, but we use the eight parameters of the redshift-dependent SHM relation that have been derived in the previous section.

The resulting interpolated SMFs are compared to the observations (and the fitted mass functions) in Figure 12. For $z \lesssim 2$, we see excellent overall agreement, the interpolated mass functions mostly overlap with the error bars of the observations.

The SMFs for the high-redshifts $z \gtrsim 2$ are too low. The deviations are largest at the low mass end. However, if we look at Figure 12, we see that β is higher than the derived value for the two highest redshifts which results in a low-mass slope that is too shallow.

To compare the relation at different redshifts, we use the redshift-dependent SHM relation with the eight parameters that have been derived in the previous section. Figure 14 plots stellar mass versus halo mass for different redshifts. The plot shows that at a fixed low halo mass (e.g., $M = 10^{11}\,M_\odot$), galaxies that live in such halos are more massive at low redshift ($m \sim 10^9\,M_\odot$ for $z = 0$) than galaxies that live in a halo of the same mass at a higher redshift ($m \sim 10^8\,M_\odot$ for $z = 2$). In contrast, massive halos contain more massive galaxies at high redshift, while at low redshifts the galaxies in massive halos have less mass. However, as halos also become more massive over time, one cannot identify a halo of a certain mass at high redshifts with a halo of the same mass at low redshifts. Thus, the fact that at a given (high) halo mass the mass of the central galaxy is lower at present than at an earlier epoch does not imply that individual galaxies lose mass during their evolution. This only means that large halos accrete dark matter faster than large galaxies grow in stellar mass, while the growth of low-mass halos is slower than that of the central galaxies they harbor (see also Conroy & Wechsler 2009). Because of its statistical nature, our model is not suitable for following the evolution of an individual galaxy through cosmic time. We also note that the SHM relation at the massive end ($M \gtrsim 10^{13}\,M_\odot$) undergoes very little evolution, which has also been found by Brown et al. (2008).

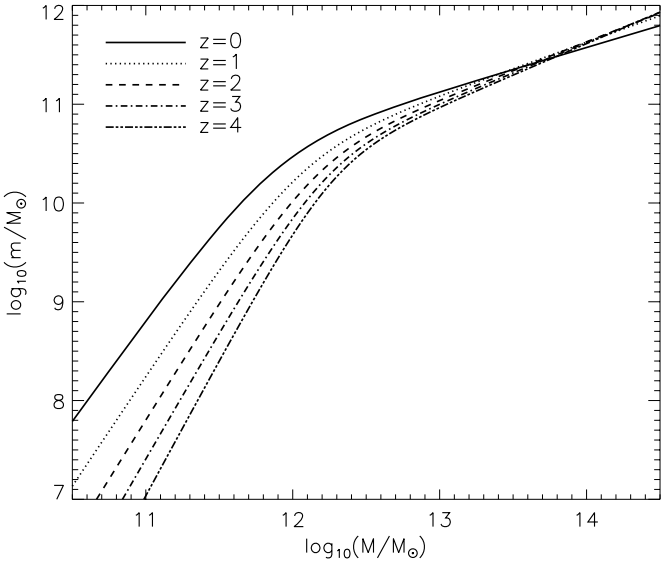

Figure 14. Stellar mass as a function of halo mass for different redshifts. The solid lines show different redshifts, which are indicated at the top of the panels.

7.4. Clustering at Higher Redshift

Having determined the SHM relation as a function of redshift, we are now able to populate halos with galaxies at any redshift.

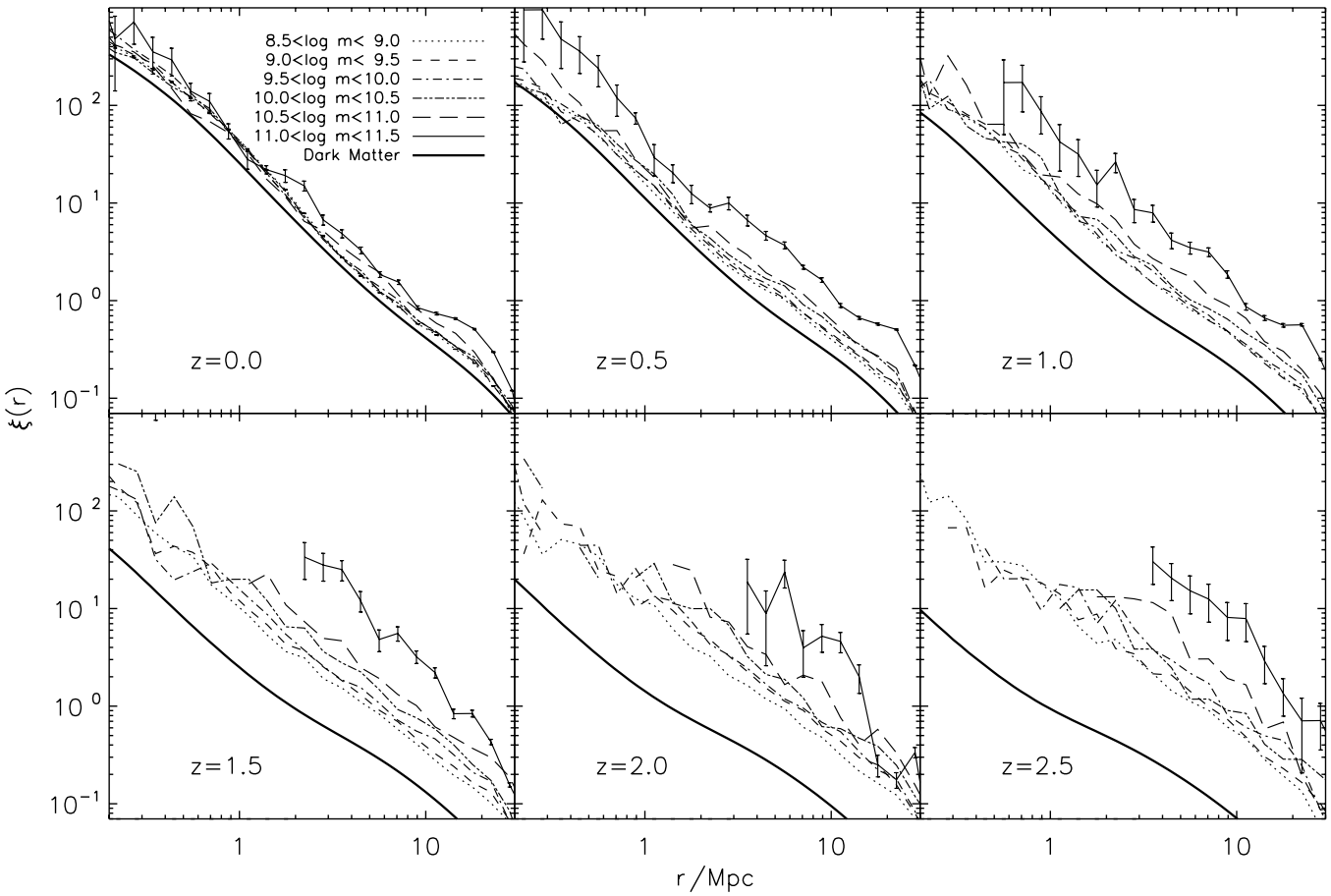

Figure 15. Correlation functions as a function of stellar mass at high redshift. The different panels correspond to different redshifts, which are given at the bottom of each panel. The different lines are correlation functions for six stellar mass bins, which are given in the upper left panel. The error bars on the most massive sample are from Poisson statistics. The correlation function of dark matter particles (thick solid line) at the respective redshifts is also shown for comparison. At high redshift, the correlation function of the massive samples is only shown on large scales, since there is no relevant one-halo term.

We choose a set of redshifts and populate the halos with galaxies, deriving the stellar masses from the redshift-dependent SHM relation. We divide these galaxies into six samples of different stellar mass between $\log m/M_{\odot} = 8.5$ and 11.5. For each of these samples, we compute the real space CF $\xi(r)$ by counting pairs in distance bins (Equation (3)). This leads to six CFs for every selected redshift.

Figure 15 shows the CFs for six different redshifts as a function of stellar mass. We also plot the correlation function of dark matter at the respective redshifts for comparison. For all redshifts, we see that massive galaxies are clustered more strongly than low mass galaxies. The higher the redshift, the more the CFs for different stellar masses differ. For high redshift, there are very few massive galaxies in our limited volume simulation box, and so the error bars become larger.

At low redshift ($z \lesssim 1$), observational measurements of stellar mass dependent galaxy clustering have recently been published using the VIMOS-VLT Deep Survey (VVDS) and the zCOSMOS Survey (Meneux et al. 2008, 2009). In order to compare our model predictions to these data, we compute correlation functions for the same stellar mass bins and thresholds and convert these to projected correlation functions as described in Section 3.2. Figure 16 plots the observed projected correlation functions (symbols) and the model predictions (lines) for different stellar mass bins or thresholds in three redshift bins for the zCOSMOS Survey and one redshift bin for the VVDS. There is good general agreement between the model and observations.

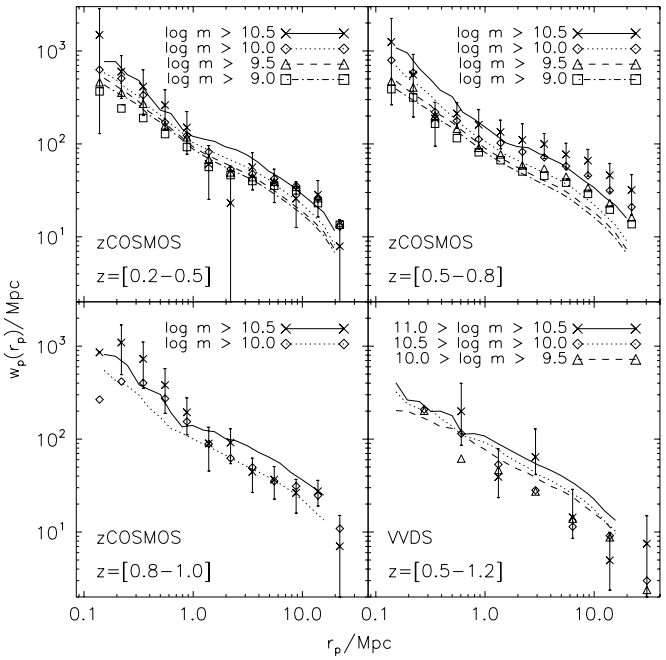

Figure 16. Comparison between the model (lines) and observed (symbols) projected correlation functions at $0.2 < z < 1.2$. The upper and the left panels show the zCOSMOS data in three redshift bins, while the lower right panel shows the VVDS data. The different lines and symbols in each panel are for different stellar mass bins and thresholds as indicated in the panels.

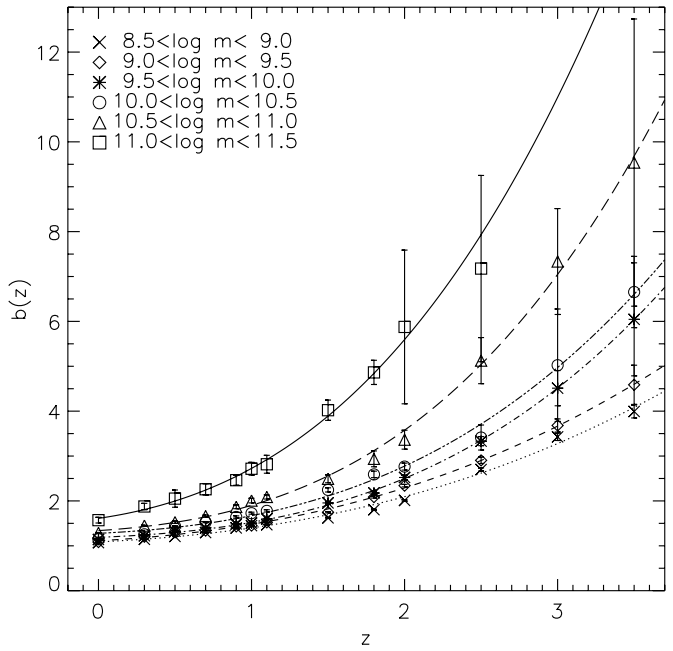

Figure 17. Galaxy bias at a fixed scale (≈ 6 Mpc) as a function of redshift for different stellar masses. The symbols have been derived by averaging the bias over a distance interval while the lines are fits to the symbols.

The zCOSMOS clustering amplitude agrees very well with the model for $r_p < 1$ Mpc, but for $z < 0.8$ deviates at larger distances and becomes higher than the prediction. As suggested by Meneux et al. (2009), this may be because the COSMOS field represents an overdense volume at these redshifts. In contrast, the VVDS clustering amplitudes are lower than those predicted by our model, leading to the speculation that perhaps the VVDS represents an underdense region.

7.5. The Galaxy Bias

The bias of any object may be defined as the square root of the ratio between the CF of the object $\xi_o(r)$ and the CF of dark matter particles $\xi_{dm}(r)$:

$$b(r) = \sqrt{\frac{\xi_o(r)}{\xi_{dm}(r)}}. \quad (27)$$

Here, we focus on the galaxy two-point CF $\xi_{gg}(r, m, z)$, which in addition to the distance between the galaxies also depends on the redshift and the stellar mass of the galaxies:

$$b(r, m, z) = \sqrt{\frac{\xi_{gg}(r, m, z)}{\xi_{dm}(r, z)}}. \quad (28)$$

From our predicted galaxy CFs, we compute the bias for every redshift and stellar mass by averaging between $r = 2$ Mpc and 10 Mpc, where $b(r)$ is roughly a constant (as one can see from Figure 15, the scale dependence of the bias is quite weak). Figure 17 shows the redshift dependence of the bias. The symbols represent the averaged value of the bias, while the solid lines correspond to a fit to the symbols. For this, we have used a power-law form:

$$b(z) = b_0(z + 1)^{b_1} + b_2 \quad , \quad (29)$$

where the parameters b_0, b_1, and b_2 are functions of stellar mass. The fit parameters are given in Table 8.

Table 8
Galaxy Bias Fit Parameters

log m_g	b_0	b_1	b_2
8.5–9.0	0.062 ± 0.017	2.59 ± 0.18	1.025 ± 0.062
9.0–9.5	0.074 ± 0.008	2.58 ± 0.26	1.039 ± 0.028
9.5–10.0	0.042 ± 0.003	3.17 ± 0.05	1.147 ± 0.021
10.0–10.5	0.053 ± 0.014	3.07 ± 0.17	1.225 ± 0.077
10.5–11.0	0.069 ± 0.014	3.19 ± 0.13	1.269 ± 0.087
11.0–11.5	0.173 ± 0.035	2.89 ± 0.20	1.438 ± 0.061

Note. All quoted masses are in units of $M_\odot$.

This shows that the bias at a fixed stellar mass increases with increasing redshift. Massive galaxies are biased more strongly than galaxies of lower mass at any redshift. We find that the bias of massive galaxies evolves more rapidly than that of low mass ones (cf. White et al. 2007; Brown et al. 2008). Since the bias of massive halos evolves more rapidly than that of low mass galaxies, this seems to be a feature of any model in which the SHM relation is monotonically increasing (i.e., the most massive galaxies reside in the most massive halos).

8. CONCLUSIONS

The goal of this paper is to characterize the relationship between the stellar masses of galaxies and the masses of the dark matter halos in which they live at low and high redshift, and to make predictions of stellar mass dependent galaxy clustering at high redshift.

We used a high-resolution N-body simulation and identified halos and subhalos. Halos and subhalos were populated with central and satellite galaxies using a parameterized SHM relation. For host halos, the mass was given by the virial mass $M_{\rm vir}$ while for subhalos we used the maximum mass of the halo over its history $M_{\rm max}$ since we expect the stellar mass of the satellite galaxy to be more tightly linked to this quantity.

We described the ratio between stellar and halo mass by a function with four free parameters, a low-mass slope β, a characteristic mass M_1, a high-mass slope γ, and a normalization $(m/M)_0$. We fit for the values of these parameters by requiring that the observed galaxy SMF is reproduced. We find that the SHM function has a characteristic peak at $M_1 \sim 10^{12}\,M_\odot$, and declines steeply toward both smaller mass ($\beta \sim 1$) and less steeply toward larger mass halos ($\gamma \sim 0.6$). The physical interpretation of this behavior is the interplay between the various feedback processes that impact the star formation efficiency. Supernova feedback is more effective at reheating and expelling gas in low-mass halos, while AGN feedback is more effective in high mass halos (e.g., Shankar et al. 2006; Croton et al. 2006; Bower et al. 2006; Somerville et al. 2008). In this picture, the characteristic mass M_1 is the halo mass where the efficiency of these two processes crosses.

We have thoroughly discussed the meaning of the parameters. We have also investigated the effects on the SHM relation that arise from introducing scatter to the relation. To do this, we have added scatter drawn from a lognormal distribution with a typical variance of $\sigma_m = 0.15$ to the SHM function. We showed that the impact of such a scatter on three of the four parameters is negligible, with a small but significant impact on the high-mass slope γ.

We showed that adding constraints from stellar mass dependent galaxy clustering did not change the values of our best-fit parameters. Put another way, the likelihood (here χ^2) function

for the clustering constraint is much "flatter" than that for the mass constraint, so adding the clustering constraint does not significantly change the distribution for the most likely (best-fit) parameter values. Fitting to the SMF only, we found that the observed projected CFs of galaxies for five samples of different stellar mass were reproduced well. This means that the clustering properties of galaxies are predominantly driven by the clustering of the halos and subhalos in which they reside. From this, we concluded that our model can predict clustering as a function of stellar mass at any redshift.

In order to describe how galaxies of different masses populate host halos, we introduced the conditional mass function $\Phi(m|M)$, which yields the average number of galaxies with stellar masses in the range $m \pm dm/2$ that live in a distinct halo of mass M. It is described by five parameters which are functions of halo mass. We divided the conditional mass function into a contribution from central galaxies (described by a log-normal distribution) and a contribution from satellite galaxies (described by a modified Schechter function). We computed the SMF in different halo mass bins and fitted the five parameters in each bin. Introducing halo mass dependent functions for every parameter and fitting these to the derived values of the parameters in the halo mass bins, we determined the halo mass dependence of the five parameters and thus fully described the conditional mass function. We also computed the occupation numbers of halos which give the average number of galaxies of a given stellar mass that live inside a halo of mass M.

We compared the results for our SHM function with those that have been derived using other approaches. These include other halo occupation type models, gravitational lensing, and SAMs. We showed that all methods yield consistent SHM relations.

Using SMFs at higher redshifts, we applied our model at earlier epochs of the universe. We thus constrained the SHM relation at a given set of redshifts between $z = 0$ and $z \sim 4$. This allowed us to study how the four parameters of the SHM function depend on redshift. For each parameter, we introduced a redshift-dependent function. We found that the characteristic mass increases with redshift while the normalization decreases with redshift. This indicates that there is less stellar content in halos at higher redshifts. As the halo mass function steepens more with redshift than the SMF, the low-mass slope increases with redshift. We present an eight parameter fitting function describing the redshift-dependent SHM relation.

Using the SHM relation that we derived in this way, along with spatial information for halos from the N-body simulation, we predicted the high-redshift real space CFs for five stellar mass intervals. We find that for all redshifts, massive galaxies are more clustered than galaxies of lower mass. Using the real space CF of dark matter, we calculated the galaxy bias as a function of distance, redshift, and stellar mass. Averaging over spatial scale in an interval around $r \approx 6$ Mpc, we demonstrated that the galaxy bias increases with redshift, and presented fitting formulae for the galaxy bias as a function of stellar mass and redshift. In a forthcoming companion paper (Moster et al. 2010), we use these bias results to present predictions for the cosmic variance σ_c for galaxies of different stellar mass.

We thank Benjamin Panter, Cheng Li, Adriano Fontana, Niv Drory, Rachel Mandelbaum, and Baptiste Meneux for providing their data in electronic form. We also thank Eric Bell, Ramin Skibba, Risa Wechsler, and Charlie Conroy for helpful discussions and Zheng Zheng, Baptiste Meneux, and Michael Brown for helpful comments on a draft version of this paper. We are also grateful to the referee whose comments improved the presentation of our work. This research was supported in part by the DFG cluster of excellence "Origin and Structure of the Universe."

REFERENCES

Bell, E. F., & de Jong, R. S. 2001, ApJ, 550, 212
Berlind, A. A., & Weinberg, D. H. 2002, ApJ, 575, 587
Bertschinger, E. 2001, ApJS, 137, 1
Blumenthal, G. R., Faber, S. M., Primack, J. R., & Rees, M. J. 1984, Nature, 311, 517
Bower, R. G., Benson, A. J., Malbon, R., Helly, J. C., Frenk, C. S., Baugh, C. M., Cole, S., & Lacey, C. G. 2006, MNRAS, 370, 645
Boylan-Kolchin, M., Ma, C.-P., & Quataert, E. 2008, MNRAS, 383, 93
Brown, M. J. I., et al. 2008, ApJ, 682, 937
Bryan, G. L., & Norman, M. L. 1998, ApJ, 495, 80
Cacciato, M., van den Bosch, F. C., More, S., Li, R., Mo, H. J., & Yang, X. 2009, MNRAS, 394, 929
Carlberg, R. G., Yee, H. K. C., Ellingson, E., Abraham, R., Gravel, P., Morris, S., & Pritchet, C. J. 1996, ApJ, 462, 32
Cole, S., Aragon-Salamanca, A., Frenk, C. S., Navarro, J. F., & Zepf, S. E. 1994, MNRAS, 271, 781
Conroy, C., & Wechsler, R. H. 2009, ApJ, 696, 620
Conroy, C., Wechsler, R. H., & Kravtsov, A. V. 2006, ApJ, 647, 201
Cooray, A. 2006, MNRAS, 365, 842
Croton, D. J., et al. 2006, MNRAS, 365, 11
Drory, N., Bender, R., Feulner, G., Hopp, U., Maraston, C., Snigula, J., & Hill, G. J. 2004, ApJ, 608, 742
Drory, N., Salvato, M., Gabasch, A., Bender, R., Hopp, U., Feulner, G., & Pannella, M. 2005, ApJ, 619, L131
Elsner, F., Feulner, G., & Hopp, U. 2008, A&A, 477, 503
Erickson, L. K., Gottesman, S. T., & Hunter, J. H., Jr. 1987, Nature, 325, 779
Eyles, L. P., Bunker, A. J., Ellis, R. S., Lacy, M., Stanway, E. R., Stark, D. P., & Chiu, K. 2007, MNRAS, 374, 910
Fall, S. M., & Efstathiou, G. 1980, MNRAS, 193, 189
Fontana, A., et al. 2006, A&A, 459, 745
Katz, N., Weinberg, D. H., & Hernquist, L. 1996, ApJS, 105, 19
Kauffmann, G., White, S. D. M., & Guiderdoni, B. 1993, MNRAS, 264, 201
Kauffmann, G., et al. 2003, MNRAS, 341, 33
Klypin, A., Gottlöber, S., Kravtsov, A. V., & Khokhlov, A. M. 1999, ApJ, 516, 530
Kravtsov, A. V., Berlind, A. A., Wechsler, R. H., Klypin, A. A., Gottlöber, S., Allgood, B., & Primack, J. R. 2004, ApJ, 609, 35
Kroupa, P. 2001, MNRAS, 322, 231
Mandelbaum, R., Seljak, U., Kauffmann, G., Hirata, C. M., & Brinkmann, J. 2006, MNRAS, 368, 715
Mandelbaum, R., Tasitsiomi, A., Seljak, U., Kravtsov, A. V., & Wechsler, R. H. 2005, MNRAS, 362, 1451
Marín, F. A., Wechsler, R. H., Frieman, J. A., & Nichol, R. C. 2008, ApJ, 672, 849
Meneux, B., et al. 2008, A&A, 478, 299
Meneux, B., et al. 2009, A&A, 505, 463
More, S., van den Bosch, F. C., & Cacciato, M. 2009a, MNRAS, 392, 917
More, S., van den Bosch, F. C., Cacciato, M., Mo, H. J., Yang, X., & Li, R. 2009b, MNRAS, 392, 801
Moster, B. P., Somerville, R. S., Newman, J. A., & Rix, H.-W. 2010, ApJ, submitted (arXiv:1001.1737)
Li, C., Kauffmann, G., Jing, Y. P., White, S. D. M., Börner, G., & Cheng, F. Z. 2006, MNRAS, 368, 21
Lin, Y.-T., & Mohr, J. J. 2004, ApJ, 617, 879
Lin, Y.-T., Mohr, J. J., & Stanford, S. A. 2003, ApJ, 591, 749
Norberg, P., et al. 2001, MNRAS, 328, 64
Norberg, P., et al. 2002, MNRAS, 332, 827
Panter, B., Heavens, A. F., & Jimenez, R. 2004, MNRAS, 355, 764
Panter, B., Jimenez, R., Heavens, A. F., & Charlot, S. 2007, MNRAS, 378, 1550
Peacock, J. A., & Smith, R. E. 2000, MNRAS, 318, 1144
Press, W. H., Teukolsky, S. A., Vetterling, W. T., & Flannery, B. P. 1992, Numerical Recipes in C (2nd ed.; Cambridge: Cambridge Univ. Press)
Seljak, U. 2000, MNRAS, 318, 203
Shankar, F., Lapi, A., Salucci, P., De Zotti, G., & Danese, L. 2006, ApJ, 643, 14
Sheth, R. K., & Tormen, G. 1999, MNRAS, 308, 119
Somerville, R. S., Hopkins, P. F., Cox, T. J., Robertson, B. E., & Hernquist, L. 2008, MNRAS, 391, 481
Somerville, R. S., & Primack, J. R. 1999, MNRAS, 310, 1087

Spergel, D. N., et al. 2007, ApJS, 170, 377
Springel, V. 2005, MNRAS, 364, 1105
Springel, V., & Hernquist, L. 2003, MNRAS, 339, 289
Springel, V., White, S. D. M., Tormen, G., & Kauffmann, G. 2001, MNRAS, 328, 726
Springel, V., et al. 2005, Nature, 435, 629
Tasitsiomi, A., Kravtsov, A. V., Wechsler, R. H., & Primack, J. R. 2004, ApJ, 614, 533
Tinker, J. L., Weinberg, D. H., Zheng, Z., & Zehavi, I. 2005, ApJ, 631, 41
Vale, A., & Ostriker, J. P. 2006, MNRAS, 371, 1173
van den Bosch, F. C., Yang, X., & Mo, H. J. 2003, MNRAS, 340, 771
van den Bosch, F. C., et al. 2007, MNRAS, 376, 841
Wang, L., Li, C., Kauffmann, G., & De Lucia, G. 2006, MNRAS, 371, 537
Wang, L., Li, C., Kauffmann, G., & De Lucia, G. 2007, MNRAS, 377, 1419
White, M. 2001, MNRAS, 321, 1
White, S. D. M., & Rees, M. J. 1978, MNRAS, 183, 341
White, M., Zheng, Z., Brown, M. J. I., Dey, A., & Jannuzi, B. T. 2007, ApJ, 655, L69
Yan, H., Dickinson, M., Giavalisco, M., Stern, D., Eisenhardt, P. R. M., & Ferguson, H. C. 2006, ApJ, 651, 24
Yang, X., Mo, H. J., Jing, Y. P., van den Bosch, F. C., & Chu, Y. 2004, MNRAS, 350, 1153
Yang, X., Mo, H. J., & van den Bosch, F. C. 2003, MNRAS, 339, 1057
Yang, X., Mo, H. J., & van den Bosch, F. C. 2008, ApJ, 676, 248
Yang, X., Mo, H. J., van den Bosch, F. C., Pasquali, A., Li, C., & Barden, M. 2007, ApJ, 671, 153
Zaritsky, D., Smith, R., Frenk, C., & White, S. D. M. 1993, ApJ, 405, 464
Zehavi, I., et al. 2002, ApJ, 571, 172
Zehavi, I., et al. 2004, ApJ, 608, 16
Zehavi, I., et al. 2005, ApJ, 630, 1
Zheng, Z., et al. 2005, ApJ, 633, 791